Lukas Holzknecht, BSc

Derived vs. in-situ measured density of coronal mass ejections

MASTER'S THESIS

to achieve the university degree of

Diplom-Ingenieur

Master's degree programme: Space Sciences and Earth from Space

submitted to

Graz University of Technology

Supervisor

Assoz. Univ.-Prof. Dr. Manuela Temmer

Co-supervisor

Dr. Mateja Dumbović

Institute of Physics
University of Graz

Graz, October 2019

Affidavit

I declare that I have authored this thesis independently, that I have not used other than the declared sources/resources, and that I have explicitly indicated all material which has been quoted either literally or by content from the sources used. The text document uploaded to TUGRAZonline is identical to the present master‘s thesis.

Date	Signature

Acknowledgement

I would like to thank Dr. Manuela Temmer not only for providing valuable help and information throughout the entire project, but also for introducing me to the great team of the insitute (IGAM). I am very grateful to have been given the chance to join conferences and workshops and gain insight to a scientists everyday life.

I also want to thank Dr. Mateja Dumbović for providing great input to numerous topics concerning this master's thesis.

A very special thank you addresses my family, who have been supporting me my entire life and without whose help my chances to study would have been largely diminished.

Abstract

Magnetic reconnection processes on the Sun trigger the most energetic eruptions in the solar system, the coronal mass ejections (CMEs). These eruptions travel through interplanetary space with speeds of up to 3000 km s^{-1} and sometimes reach the Earth. There they interact with the Earth's protecting magnetosphere and may cause space weather effects. Being an important parameter for the drag force acting on the CME, its density is to be studied in detail. From combined stereoscopic white light images of the STEREO SECCHI instruments we derive both the CME's volume and its 3D excess mass at around 15 $R_{\odot}$. Hence, the excess density is obtained by dividing mass over volume. Assigning the CME to its interplanetary counterpart (ICME) as measured in-situ near Earth we assume that the CME consists of the same measured parts. That is its frontal part with the leading shock front (ICME shock-sheath region) and the flux rope part (ICME magnetic ejecta region) where we assume the entire excess mass to be located. In the frontal part, however, the CME piles up available mass in interplanetary space provided by the solar wind. One can exemplary think of a snow plough piling up snow in front of it. The results of this thesis show that it is not possible to numerically predict the density evolution mainly due to the large uncertainties of the subjective reconstruction from white light images. Nevertheless, the results of this thesis are strongly supporting the above stated assumptions (excess mass in flux rope part stays constant and shock-sheath mass refers to piled up solar wind material).

Kurzfassung

Magnetische Rekonnexionsprozesse auf der Sonne verursachen die energiereichsten Eruptionen im Sonnensystem, die sogenannten Koronalen Massenauswürfe (englisch coronal mass ejection, CME). Diese Eruptionen breiten sich mit Geschwindigkeiten bis zu 3000 km s^{-1} aus und können auch die Erde erreichen. Dort interagieren sie mit dem, die Erde schützenden, Erdmagnetfeld und können sich auf das Weltraumwetter auswirken. Ein wichtiger Parameter in Bezug auf den aerodynamischen Widerstand des CMEs stellt die Dichte dar. Um die Geometrie (bzw. das Volumen) sowie die Initialmasse des CMEs zu bestimmen, werden stereoskopische Weißlichtbilder der Koronografen der STEREO SECCHI Instrumente verwendet. Im Abstand von ca. 15 Sonnenradien wird die Dichte über die einfache Beziehung - Initialmasse geteilt durch Volumen - berechnet. Infolgedessen wird dem CME sein interplanetares Gegenstück, der sogenannte ICME (englisch für interplanetary coronal mass ejection), zugewiesen. In-situ Plasma- und Magnetfeldmessungen nahe der Erde zeigen charakteristische Signaturen, welche den CME in unterschiedliche Abschnitte einteilen lassen. Der vordere Bereich ist der sogenannte shock-sheath Bereich, während der zweite Teil die magnetische Flussröhre ist, welche vermeintlich die gesamte Initialmasse beinhält. Im Zuge dieser Arbeit wird angenommen, dass der Anteil der Masse (und daher auch der Dichte), welcher in-situ im shock-sheath Bereich gemessen wird, unabhängig von der restlichen Masse (also jener im Flussröhrenbereich) ist. Diese Masse kommt daher zustande, da der CME auf seiner Reise durch das interplanetare Medium Masse, die ununterbrochen von der Sonne ausgesandt wird (der sogenannte Sonnenwind), vor sich aufstaut. Dieser Effekt ist mit einem Schneepflug, der den Schnee vor sich aufstaut, vergleichbar. Die Resultate dieser Arbeit weisen darauf hin, dass sich korrekte Vorhersagen über den Verlauf der Dichte eines CMEs zahlenmäßig nicht ableiten lassen, da das subjektive Rekonstruieren anhand von Weißlichtbildern mit großen Unsicherheiten behaftet ist. Dennoch konnte in dieser Arbeit gezeigt werden, dass die oben genannten Annahmen (Masse in der Flussröhre bleibt konstant und Masse im shock-sheath Bereich beinhält aufgestautes Sonnenwindmaterial) angemessen erscheinen.

Contents

1 Introduction

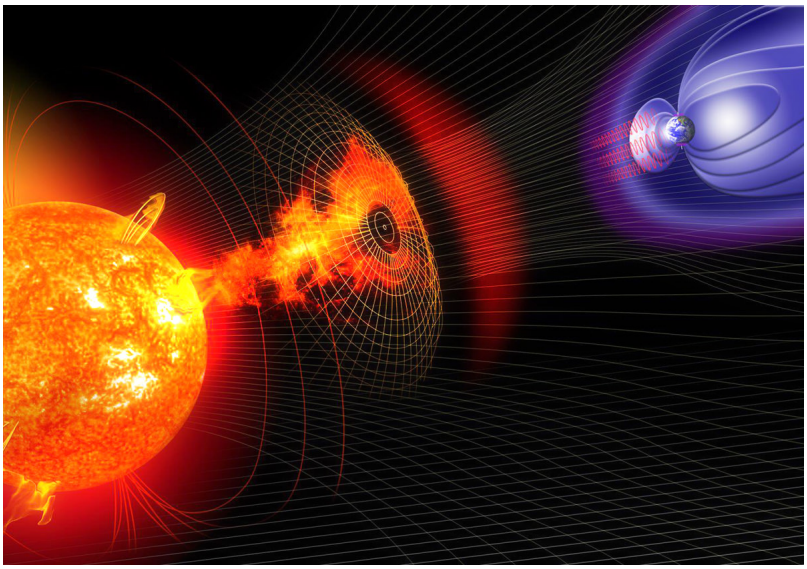

Figure 1.1: Artificial representation of an Earth directed coronal mass ejection. *Credit*: NASA.

The Sun is the largest object and the centre of our solar system. It is the driving force for many phenomena happening on and around the Earth and thus it is an object worth studying. Its continuous stream of plasma, known as the solar wind, emanating from the upper part of the solar atmosphere, hits the Earth and every other planet. Depending on the solar activity, which is closely related to variations in the magnetic field of the Sun, the solar wind can vary in speed and strength. The strongest form of matter release from the Sun are coronal mass ejections (CMEs). CMEs arrive at Earth within less than a few days and can cause severe disturbances in the Earth's environment. Gosling (1993) found that CMEs are mainly responsible for geomagnetic disturbances. Figure 1.1 gives an artificial representation of an Earth directed CME. The permanent bombardment of matter and magnetic field and its effects on a planet's magnetosphere and outer atmosphere is referred to as space weather. Space weather can have multiple manifestations such as satellite damage through accelerated particles, satellite communication problems (navigation systems, etc.) or high radiation exposure to astronauts or airplane crews and passengers in high altitude flights. A very famous and also beautiful example of the interaction between solar wind particles and the Earth's atmospheric constituents are the Northern Lights (see Figure 1.2).

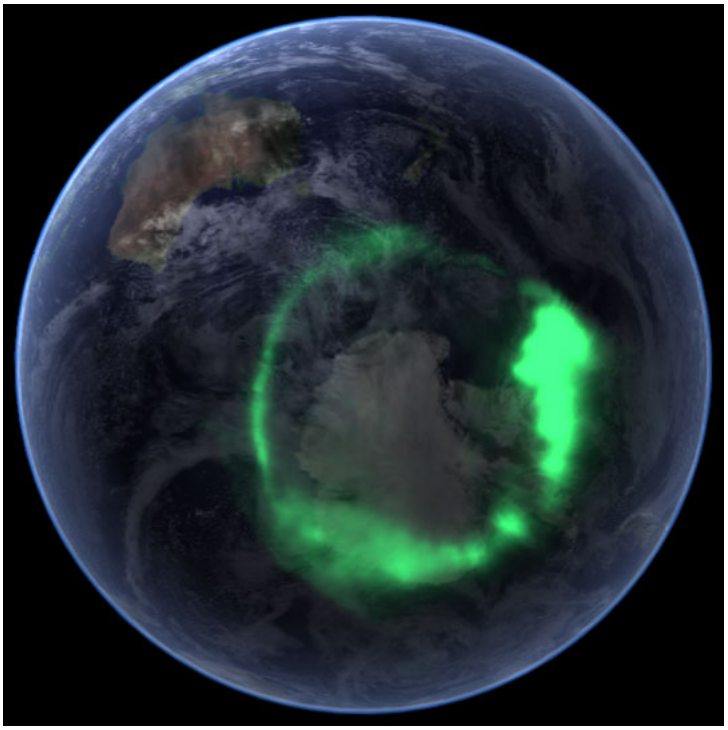

Figure 1.2: Aurora australis seen from space taken by the IMAGE satellite on 11 September 2005. *Credit*: NASA.

Happening on both the northern and southern pole regions at certain latitudes, this natural phenomenon is a decent indicator for the Sun's influence on the Earth's magnetic field. CMEs can either be detected remotely with white-light imaging of so-called coronagraphs (explained in a later chapter) or via in-situ measurements. For the latter, spacecraft parked at certain positions outside the Earth's magnetosphere constantly measure the plasma flow. Within those measurements CMEs leave a certain footprint which is to be seen by sudden enhancements in plasma parameters such as velocity, magnetic field, temperature or density followed by specific magnetic field characteristics.

Hence, the solar wind and CMEs, are to be studied in detail. Forecasting such events can be crucial in terms of preventive actions to be taken. Besides the speed that gives information on the arrival time of the CME, the CME's density is another important parameter relevant for the drag force exerted on the CME when propagating in interplanetary space (Vršnak et al., 2004, 2013). We will investigate on the CME's mass propagation in interplanetary space and address yet unresolved questions such as the evidence of mass pile up in front of the CME. Furthermore, this thesis focuses on how the density is related to other parameters and whether we can estimate the incoming particle density of CMEs only by reconstructing their geometry from white-light images (Thernisien et al., 2006, 2011). By comparing theoretical assumptions derived from remote sensing data with actual in-situ measurements we want to draw conclusions whether or not our assumptions are reasonable.

2 The Sun, solar wind and coronal mass ejections

2.1 The Sun

The nearest star to Earth, the Sun, is an object that has ever been of great essentiality for every process on Earth. It provides energy since the very beginning of our planet and drives all natural cycles. Its distance to Earth enables water to be liquid which is a very important fact that life, as we know it, could arise. It is the only star we can observe the surface in detail, since the astronomical distances to other stars are too far. The second nearest star, Proxima Centauri, is already about 1.3 pc (pc for parallax second; 1 pc = 30.857×10^{15}m) or 4.2 ly (ly for lightyear; 1 ly $\approx 9.46 \times 10^{15}$m away).

The activity of the Sun is primarily dominated by the magnetic field produced by the solar dynamo. Representing regions of enhanced magnetic field flux sunspots are a known indicator for the solar activity. The number of sunspots shows an 11-year cycle with an interesting movement of the spots from mid-latitudes at the beginning of each cycle to the equator as the cycle continues (Charbonneau, 2014). As of 1755 reasonable counts have been made, which is why we are currently (October 2019) situated at the end of solar cycle 24 (Kane, 2002).

The Sun's median distance to Earth is approximately 150 million kilometres and is the foundation of the astronomical unit (1 AU = 1.496×10^{11} m). Its mass is about 1.99×10^{30} kg and thus exceeds 700 times the total mass of all planets of the solar system and its radius $R_\odot$ is about 6.69×10^5 km. With a luminosity of 3.84×10^{26} W the Sun is the brightest object at daytime. The main constituents are the elements hydrogen and helium and some ppm (parts per million) of oxygen, carbon, neon, nitrogen among others. The structure of the Sun can be divided into a core, where nuclear fusion processes generate energy, after which follows the radiation zone, the convection zone and eventually the solar atmosphere (Hanslmeier, 2007). The solar atmosphere itself consists of four separate layers:

- The **photosphere** of the Sun starts at the region where light is absorbed considerably. It is about 400 km thick and therefore accounts for about 0.06% of the solar radius. The temperature in this layer decreases from 6000 K at the inner boundary to about 4500 K at the outer margin. The

Figure 2.1: The Sun close to the maximum phase during a solar eclipse, 1999 in France. The white extending structure depicts the solar corona. The red features on the limb, however, are so-called prominences. These chromospheric features can reach heights of about 40,000 up to 10^5 km with a length of several 100,000 km. Original image by Luc Viatour.

density increases inwards from roughly 10^{15} particles of hydrogen per cm^3 at the outermost to 10^{17} particles per cm^3 at the innermost part of the photosphere. More than 90% of the visible light and more than 99% of the Sun's total light and heat emerges from this layer (Foukal, 2004). Thus, the solar photosphere is observable in the visible region of the solar spectrum. In this region one can see strong absorption lines such as the H_α or the Fe I line. Notice, that in higher layers of the solar atmosphere we will find Fe lines as well. But those are ionized ones.

- The **chromosphere** is the layer of the solar atmosphere that follows outwards to the photosphere. The temperature, after reaching the minimum at the outer boundary of the photosphere, starts to rise at this very point from roughly 4,500 K to several 10,000 K. It is observable during solar eclipses or in narrow-band filters at emission lines (Ca II H and K, H_α).
- The **transition region** lies between the chromosphere and the corona where the temperature even more rapidly rises until the coronal temperature of about 10^6 K is reached. The mechanisms behind this sudden outward increase in temperature are yet to be resolved (cf. coronal heating problem).
- The **corona** is the outermost layer of the Sun

2.1.1 The solar corona

Due to the fact that the corona has a brightness of about 10^{-6} times that of the photosphere, observations with the naked eye or classical solar tele-

scopes are impossible. Before the first coronagraphs (using white light and an occulter disk to obscure the bright photospheric structures) were built, the corona was observed during solar eclipses as the bright structure around the occulted sun (see Figure 2.1). The shape of the corona is defined by the solar activity. While it is elongated symmetrically around the equator during minimum, it appears symmetrically around the entire occulted disk during solar maximum. (cf.Figure 2.1; Cranmer, 2009). Its plasma contains of highly ionized protons and electrons with temperatures of about 10^6 K. During the eclipse on the 7 August 1869 both Charles Augustus Young and William Harkness independently observed a green line at 530.3 nm. The corresponding element to this forbidden line could not be found. Therefore it was given a new name, called Coronium. Later research showed that this line is the emission line of Fe XIV (The roman numeral denotes the ionization degree, e.g. Ca XII has lost 12 -1 = 11 of its electrons). These high ionization degrees give evidence to the enormous temperatures in this region of the solar atmosphere. As knowledge and technology improved, space missions provided new opportunities to study the solar corona in other spectral ranges like the UV, EUV or via broad-band soft x-ray photographs. These methods have the advantage to not be delimited to limb observations but rather to be able to observe the corona on the solar disk (see Figure 2.2; Aschwanden, 2005). Beyond around 10^5 km above the limb, observations in radio wavelengths provide information.

Due to the corona's different light emittance or scattering, one can structure the corona into different parts. The *F-corona* (F for Fraunhofer) represents the part of the corona where dust scatters the photospheric light with the result of Fraunhofer absorption lines. In the *K-corona* (K for kontinuierlich which is german for continuous) light is Rayleigh scattered by free electrons which results in a dopplerbroadened blurred continuous spectrum. The emission corona (E-corona) is the coronal part where highly ionized elements produce emission lines (Foukal, 2004).

Coronal structures

To better understand the structural behaviour of the corona we introduce the so-called plasma β. This parameter is a mathematical description of whether the magnetic field or the surrounding plasma dominates the movement of each other. It is calculated by:

$$\beta = \frac{nk_BT}{B^2/2\mu_0} \tag{2.1}$$

where the numerator denotes the thermodynamic plasma pressure with the number density n, the Boltzmann constant k_B and the plasma temperature T. The denominator represents the magnetic pressure with the magnetic induction B and the magnetic field constant μ_0. The corona is governed by a plasma β that is lower than unity. Thus, the magnetic field dominates the motions of the plasma material.

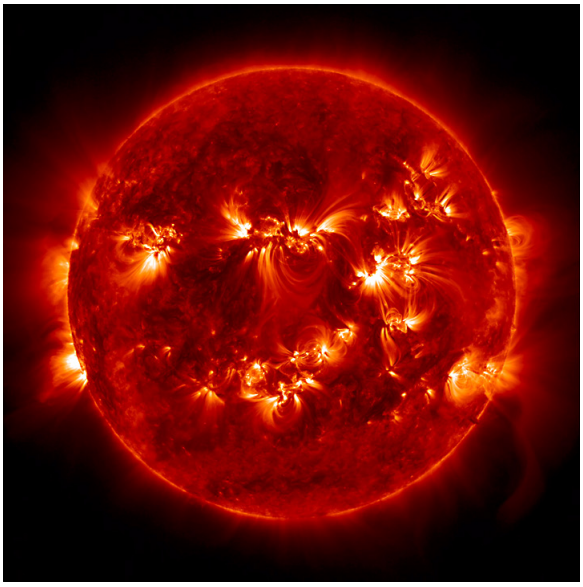

Figure 2.2: Image taken from the Atmospheric Imaging Assembly instrument (AIA; Lemen et al., 2012) onboard the *Solar Dynamics Observatory* (SDO) in the 171 Å wavelength (Fe IX line). The bright features depict active regions. *Credit*: SDO, NASA.

Coronal loops are huge plasma structures aligned with magnetic loops that are connected over large distances. Typically *coronal loops* last for days or weeks while some of them, potentially denser, can form solar flares (cf. Chapter 2.3) only having a lifetime of around ten minutes. (Hanslmeier, 2007).

Another cap-like structure called *helmet streamer* is found in active regions and over sunspots where magnetic loops connect those spots. Usually one can see a large prominence within this region.

Especially during activity minimum the intensity near the solar poles is depressed. In this region one can see *coronal holes* (CHs, see Figure 2.3). CHs are phenomena closely related to open magnetic field lines. The term "open" field lines in this context, however, does not violate one of the most fundamental equations in plasma physics $\nabla \cdot \mathbf{B} = 0$ (field lines are closed, there are no magnetic monopoles). Much rather it means that the closure of the field lines can not be observed in interplanetary space. These open field lines enable an outflow of plasma material which is why CHs are characterized by low density, pressure and temperature (Cranmer, 2009). They can account for 20% of the entire surface during activity minimum appearing predominantly near the poles. CHs can be found at all latitudes during maximum solar activity. They are observable in EUV lines such as the Fe IX line at 171 Å (cf. Figure 2.2) or e.g. the Mg X line at $\lambda = 625$ Å.

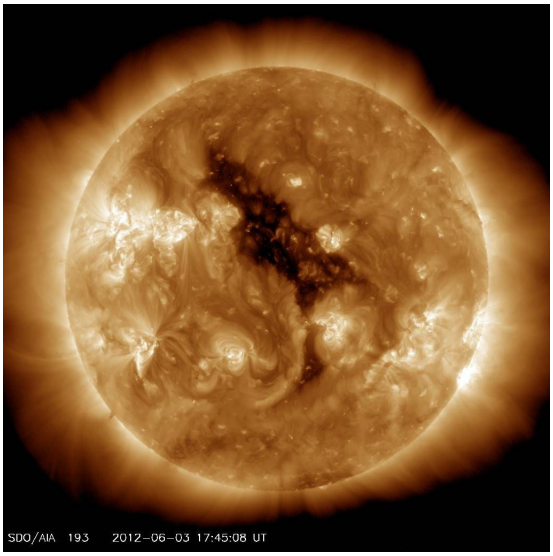

Figure 2.3: Image from 3 June 2012 taken by AIA aboard SDO depicting a coronal hole as the large black structure in the upper center of the disk. *Credit*: NASA/AIA.

2.2 The solar wind

The solar wind is a continues stream of particles that is responsible for the Sun's annual mass loss of about $2{\times}10^{-14}$ solar masses ($M_\odot$) (Aschwanden, 2005). In 1951 Biermann (1951) recognized the connection between comet tails and a seemingly permanent particle stream from the Sun. Observations led him to the conclusion that the Sun produces a continuous mass flow in all directions even at low solar activity. Measurements outside Earth's magnetosphere as part of the Mariner 2 space mission could confirm his assumptions and velocity estimations (Neugebauer and Snyder, 1966). A few years after Biermann's work, Parker (1958) developed a dynamic model of an ionized gas mainly consisting of protons and electrons, that is permanently streaming outwards from the solar atmosphere. The main difference to earlier models like the one of Chapman and Zirin (1957) was Parker's assumption of the corona not to be in hydrostatic equilibrium. The underlying considerations of an expanding corona consist of the following hydrodynamic model:

$$\frac{d}{dr}(r^2 n v_\mathrm{r}) = 0 \tag{2.2}$$

$$m_\mathrm{p} n v_\mathrm{r} \frac{dv_\mathrm{r}}{dr} = -\frac{dp}{dr} - \frac{G m_\mathrm{s} m_\mathrm{p} n}{r^2} \tag{2.3}$$

with the distance r, the density n, the velocity v_r, the pressure r, the mass of the Sun m_s and the proton mass m_p (Parker, 1960). His model predicts reasonable values for both velocity and density in accordance with Biermann's work, which posed a problem in Chapman's model. Additionally Parker introduced the term *solar wind* which has been used ever since (Parker, 1958).

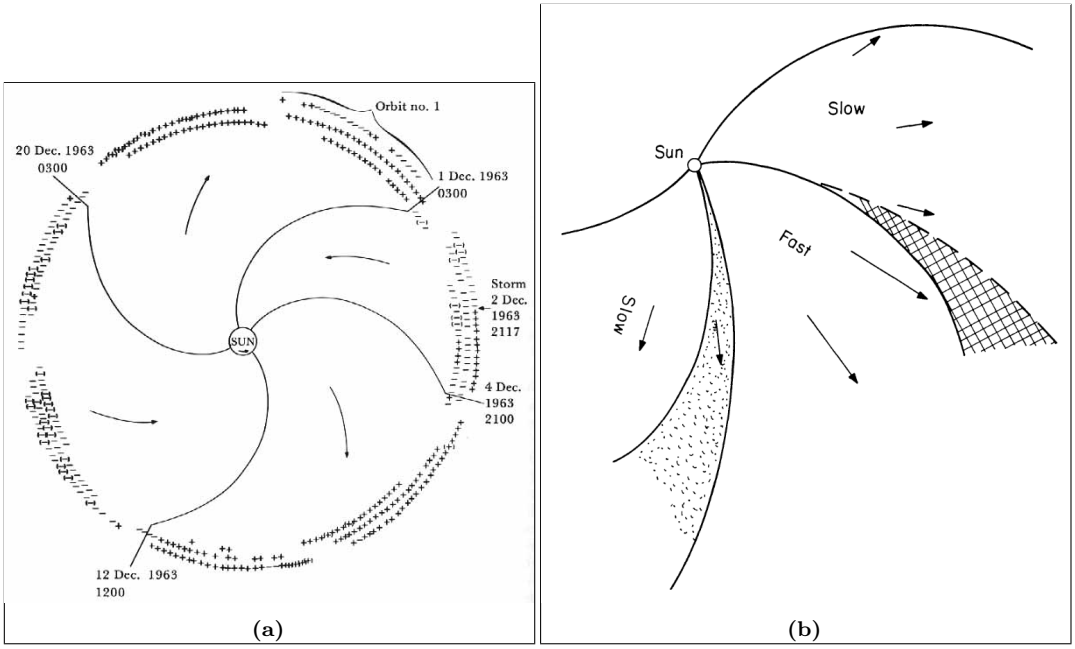

Figure 2.4: Left panel: Sketch is based on the measurements of the IMP 1 satellite and shows the interplanetary magnetic field and its archimedean spiral structure. The arrows illustrate the magnetic field lines pointing towards (-) and away (+) from the Sun. The sector boundaries are also associated with different stream velocities of the solar wind. From Wilcox and Ness (1965). Right panel: Sketch to indicate the sector boundaries with accompanying features. From Parker (1965).

Due to the high conductivity (almost zero resistivity) of the coronal plasma and the solar wind's strong connection to open field lines, the magnetic field is carried outwards with the plasma. Hence, the magnetic field is *frozen-in* the plasma. The influence of the solar rotation on the magnetic field together with the frozen-in phenomenon creates a characteristic three dimensional spiral structure. This structure is often referred to as the Parker spiral and forms the interplanetary magnetic field (IMF). Together with the frozen-in solar wind it creates the largest structure in the solar system, the heliospheric current sheet. As the solar wind's density decreases roughly with $n \sim 1/r^2$ one can find an outer boundary at about 120 AU where the interstellar medium stops the thinned out solar wind and the heliosphere turns into the heliopause (Rankin et al., 2019).

The angle ψ between the direction of the interplanetary magnetic field B_{IMF} and the Sun's outward radial direction is calculated by:

$$tan(\psi) = \frac{\omega r}{v_{\mathrm{SW}}} \tag{2.4}$$

with the angular velocity of the solar rotation $\omega = 2.68 \times 10^{-6}$ rad s^{-1}, the distance to the Sun r and the velocity of the solar wind v_{SW}. Inserting typical values for 1 AU gives an angle ψ of about 45° between B_{IMF} and the radial direction r (Raith, 2001). Due to the offset of an ideal dipole and the dipole

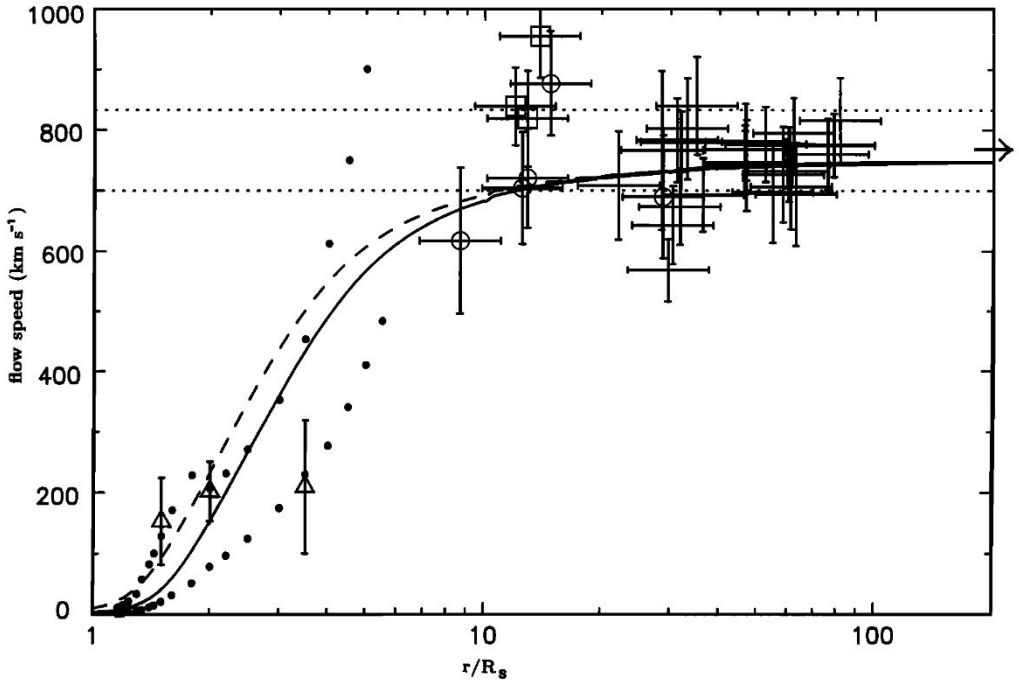

Figure 2.5: Speed profile of the HSS indicating a huge acceleration in the early propagation phase. From Esser et al. (1997).

axis' tilt to the solar rotation axis the three dimensional representation of the Parker spiral reminds of a ballerina skirt, which it is also sometimes referred to as in literature (Mursula and Virtanen, 2012; Riley et al., 2002). The polarity of the IMF changes with the Sun's rotation rate of about 27 days.

The sector boundaries (cf. Figure 2.4) mark regions where the solar wind parameters undergo fundamental differences. In contrast to the thermally driven solar wind as it was derived from Parker's model, Krieger et al. (1973) found CHs to be the source of a fast solar wind, i.e. the *high speed stream* (HSS), while the slow solar wind departs from above active regions (Schwenn, 2006). Due to the latitude dependence of active and inactive regions of the solar corona, the HSS has its origin at higher latitudes, whereas the slow solar wind originates from lower latitudes. This fact was the result of the *Ulysses* (Wenzel et al., 1992) space mission, which, in contrast to most of the other spacecraft that are parked in an ecliptic plane, was built to study the Sun at higher latitudes. Table 2.1 gives the differences of the two main types of solar winds. The slow solar wind can be subdivided into the low speed solar wind of minimum type (LSM; as listed in Table 2.1) and the low speed solar wind at high solar activity (LSA) (Schwenn, 2006). The main difference can be found within the helium abundance, which has a variable 2% at LSM and up to 4 % at LSA. About 95% of the ions in the solar wind are protons, alpha particles and heavier species represent the other 5% (Bochsler, 2009).

A still strongly discussed and yet unsolved topic is the acceleration mechanism

Table 2.1: Physical properties of the two main types of solar wind averaged as measured at 1 AU. From Schwenn (2006).

	Low speed wind (LSM)	Fast solar wind (HSS)
Flow speed v_p	250-400 km s^{-1}	400-800 km s^{-1}
Proton density n_p	10.7 cm^{-3}	3.0 cm^{-3}
Proton flux density $n_\mathrm{p}v_\mathrm{p}$	3.7×10^8 cm^{-2} s^{-1}	2.0×10^8 cm^{-2} s^{-1}
Proton temperature T_p	3.4×10^4 K	2.3×10^5 K
Electron temperature T_e	1.3×10^5 K	1.0×10^5 K
Momentum flux density	2.12×10^8 dyn cm^{-2}	2.26×10^8 dyn cm^{-2}
Total energy flux density	1.55 erg cm^{-2} s^{-1}	1.43 erg cm^{-2} s^{-1}
Helium content n_α/n_p	2.5%, variable	3.6%, stationary

that is responsible for the high velocities of the HSS. Figure 2.5 shows the velocity profile of the HSS with respect to increasing distance. Theories trying to explain the additional energy input consist of the dissipation from waves, such as magnetohydrodynamic waves like Alfvén or magnetosonic waves. Those are oscillations along (Alfvén) and perpendicular to (magnetosonic) magnetic field lines. The corresponding characteristic velocities of information transmission are the Alfvén velocity:

$$v_\mathrm{A} = \frac{B}{\sqrt{\mu_0 \rho}} \tag{2.5}$$

with the magnetic field B, the vacuum permeability μ_0 and the mass density of the charged particles ρ and the speed of sound:

$$v_\mathrm{S} = \sqrt{\frac{c_p}{c_v} \cdot \frac{p}{\rho}} \tag{2.6}$$

with the specific heat capacities c_p (constant pressure) and c_v (constant volume) and the pressure p. Regarding the bulk velocity v_SW of the solar wind and typical values for these two velocities in the interplanetary medium one finds Mach numbers ($M_\mathrm{A} = v_\mathrm{SW}/v_\mathrm{A}$) of about 10. Thus, the solar wind represents a super-sonic stream (Raith, 2001).

2.3 Coronal mass ejections

With masses of 10^{15} up to 10^{16} g and speeds beyond 2000 km s^{-1} CMEs are the most energetic events in the entire solar system. Like the solar wind they release plasma and magnetic field from the Sun. However, CMEs reveal much larger helium abundances (Yermolaev et al., 2018).

CMEs are observable either remotely through so-called coronagraphs or via their specific in-situ plasma signature (see subsection ICMEs). Coronagraphs use a disk to occult the sunlight of the photosphere, in order to observe the optically much thinner corona. CMEs are visible with these white-light images

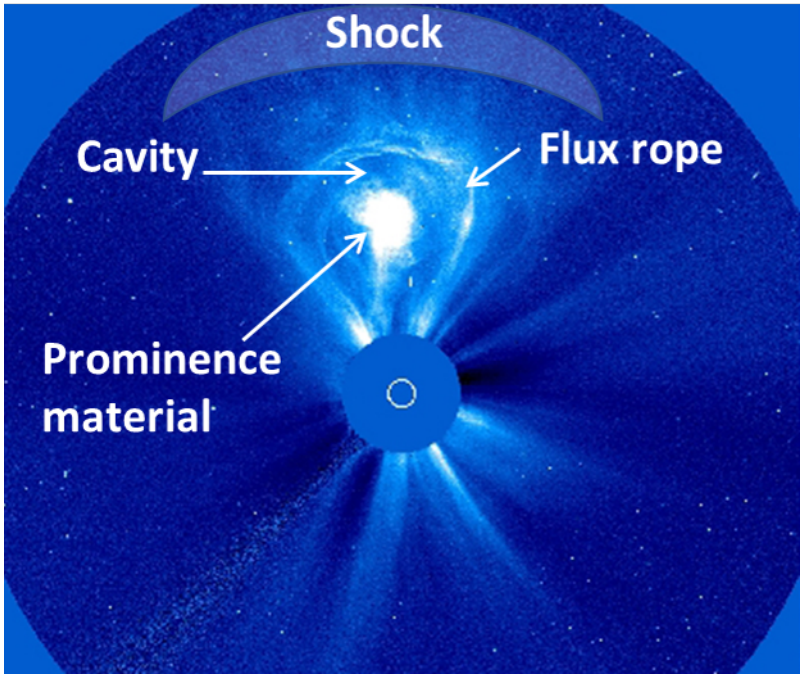

Figure 2.6: CME from 27 February 2000 observed with LASCO C3 (cf. Chapter 3) showing the typical 3-part structure as from the *standard flare-CME* model (Priest and Forbes, 2000). The size of the Sun is drawn as a white circle within the occulting disk. Adapted from Schwenn et al. (2005).

because light of the photosphere is scattered by the electrons of the CME. The underlying process is the so-called Thomson scattering, a special case for Compton scattering for low photon energy. Thomson scattering describes an elastic collision between photons and electrons. Consequently the energy that is emitted by the accelerated electrons is the same as the incident one. A very important feature one has to keep in mind is that this process is exposed to projection effects (discussed later in this thesis) as a 3-dimensional structure, namely the CME, is projected to the plane of sky (Burkepile et al., 2004; Cremades and Bothmer, 2004). The equations of Thomson scattering are also used to estimate the electron density and thus provide an important tool for the later needed CME mass calculation (see Chapter 4.1.2).

A data set of almost 1300 CMEs was used by Hundhausen (1993) to determine the apparent central latitude to be roughly distributed symmetrically along the Sun's equator with a root-mean-square average latitude of 35°. Also, they found a strong correlation with solar activity. During minimum activity the CME footpoints seem to be located near the equator, whereas their occurrence during activity maximum spreads over a wide range of latitudes. Yashiro et al. (2004) found a typical occurrence of one CME per day during activity minimum and around five CMEs per day during solar maximum. Figure 2.6 shows the typical 3-part setup with the CME's *leading edge* followed by the *cavity* and a bright kernel, the *prominence*, within the cavity. In Figure 2.7 one can see a typical white-light difference image (a previous image is subtracted from the

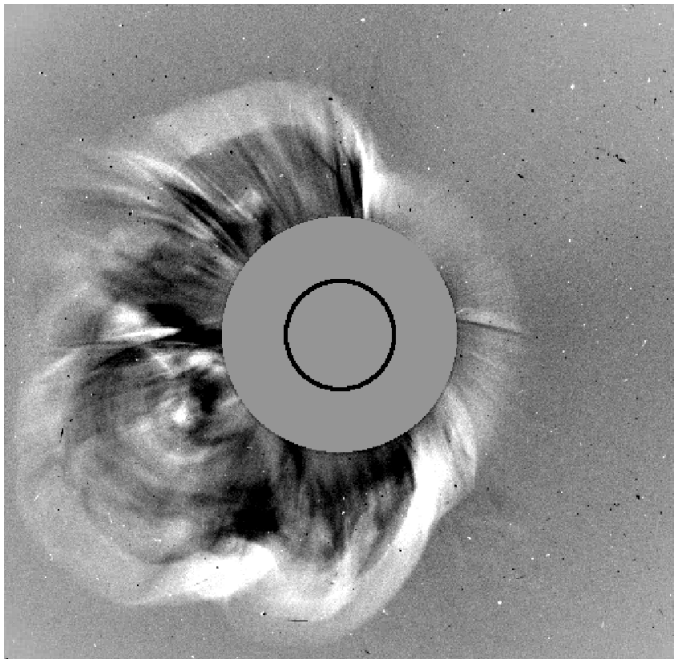

Figure 2.7: Difference image of the 28 September 2012 halo CME as seen from LASCO C2 (*Credit:* ESA/NASA SOHO LASCO CME Catalogue).

subsequent image in order to see changes and thus movements) of a so-called *halo* CME. Howard et al. (1982) assigns the term halo because of the partially or entirely brightness surrounding the occulter. The geometry indicates that the CME is either directed towards or away from the observer.

A rather large discussion within the scientific community has posed the relation between solar flares and CMEs. Like CMEs, solar flares are related to magnetic reconnection processes on the Sun. They are therefore both consequences of the same processes, however, the detailed relation is still under study. It is an established fact that most of the CMEs occur together with flares. But there are also flares without CMEs (confined flares) and CMEs without flares (stealth CMEs). On average, the more energetic the flare the higher the probability that a CME is associated.

Flares are sudden increases of the total flux and brightness, can heat up and accelerate particles into space. Usually they are observed in soft X-rays (with low energy between 0.1 and 0.8 nm), EUV or chromospheric and coronal lines. In contrast to CMEs, they happen at much smaller spatial scales and their effects on space weather due to energetic particles occur much earlier since they travel almost at the speed of light. The general mechanism of the formation is as follows: The closure of magnetic field lines adds poloidal flux to an existing flux rope (cylindrical geometry containing magnetic field Lepping et al., 1990) or builds one. The increasing magnetic pressure subsequently leads to an eruption. After this eruption magnetic reconnection with upper coronal magnetic field will decrease the magnetic tension that triggered the instability. Within this process large amounts of energy can be released that can be observed as a

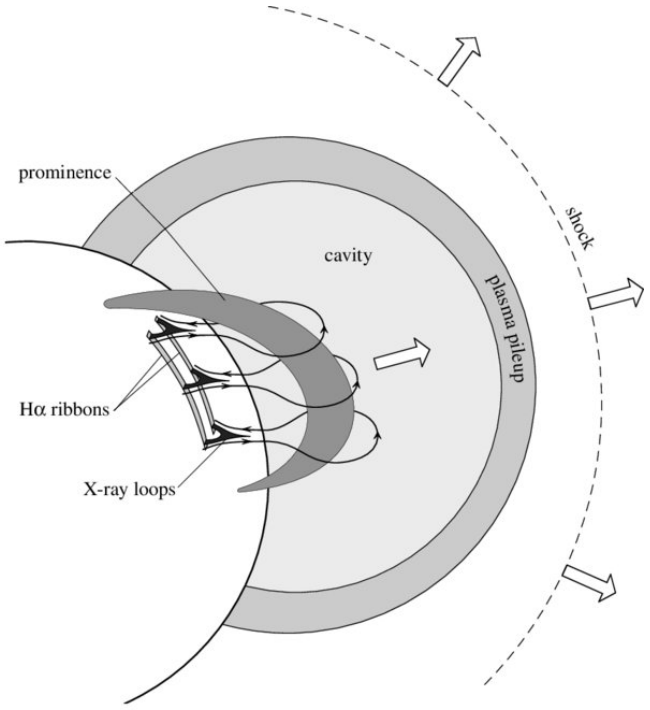

Figure 2.8: Schematic representation of the formation of an erupting magnetic structure with its accompanying features. From Priest and Forbes (2000).

solar flare has erupted (Priest and Forbes, 2000). In the outward direction the onset of the flux rope as it erupts can be super-sonic and therefore initiate shocks. The entire process forms the basis of the *standard flare-CME* model illustrated in Figure 2.8. Still, since only a part of all CMEs can be associated with the aforementioned process and discrepancies with the energy need to overcome the magnetic field of the corona (ibid.), there has to be another formation mechanism. Yashiro et al. (2005) performed a study on the CME association with 1540 X-ray flares. They confirmed that the association rate clearly increased with increasing X-ray intensity. For the highest intesity flares (X-Class flares) they found a CME association rate above 80%.

2.3.1 Interplanetary CMEs (ICMEs)

As CMEs erupt from to the Sun they start their journey through the interplanetary space. This heliospheric counterpart is called ICME. They are observable remotely through so-called heliospheric imagers (e.g. the HI instrument as part of the SECCHI instrument suite aboard NASA's twin STEREO spacecraft; Howard et al., 2008a) or in-situ by their special plasma signatures. Finding the associated CME, presents a very difficult task, as one has to make certain kinematical assumptions which might or might not be true. Zhang et al. (2001) divided the kinematical evolution of the CMEs into three different phases. An initial phase with low speed of about 80 km s^{-1} followed by an impulsive

acceleration phase and finally the propagation phase which is characterized by an almost constant speed. In this thesis we will mainly have a look at the propagation phase. After the early propagation phase at several solar radii the CME motion becomes predominantly dominated by the drag force and less by the Lorentz force (Howard, 2011). An established theory describing the CME's propagation in interplanetary space poses the aerodynamic drag model (Cargill, 2004; Vršnak et al., 2004). The general equation for the acceleration reads:

$$\frac{d^2r}{dt^2} = -\gamma(r)\left(\frac{dr}{dt} - v_{SW}(r)\right)\left|\frac{dr}{dt} - v_{SW}(r)\right| \tag{2.7}$$

with the instantaneous ICME speed v_{ICME}, the velocity of the solar wind v_{SW} and the drag parameter:

$$\gamma = \frac{c_{\mathrm{d}} A \rho_{\mathrm{SW}}}{M + M_{\mathrm{V}}} \tag{2.8}$$

with the dimensionless drag coefficient c_{d} (Cargill, 2004), the cross-section area A, the solar wind density ρ_{SW}, the initial CME mass M and the so-called *virtual mass* $M_{\mathrm{V}} \sim \rho_{\mathrm{SW}} V_{\mathrm{ICME}}/2$. This virtual mass is a measure for the mass that is available from the solar wind in the heliosphere and in further consequence can be piled up in front of the ICME. We will have a look at this parameter in more detail in Chapter 4.1.4. This model is a representation of momentum transfer between the ambient solar wind and the ICME under study. Thus, faster CMEs will slow down while slower CMEs will speed up both until they reach the speed of the surrounding solar wind. One also has to bear in mind the possibility of multiple CMEs during one day. Also, assigning the right CME often reveals discrepancies among different authors. This study uses the CME-ICME list provided by Richardson and Cane (2010).

Figure 2.9 shows an ICME detected in the in-situ measurements of the *Wind* spacecraft (see Chapter 3.4). As already mentioned, shocks can be formed in case the propagation is higher than the speed of information transmission. Hence, if the CME speed exceeds the surrounding solar wind magnetosonic speed a discontinuity is formed in front of the CME's flux rope. This shock comes along with a sudden enhancement in all measured plasma parameters.

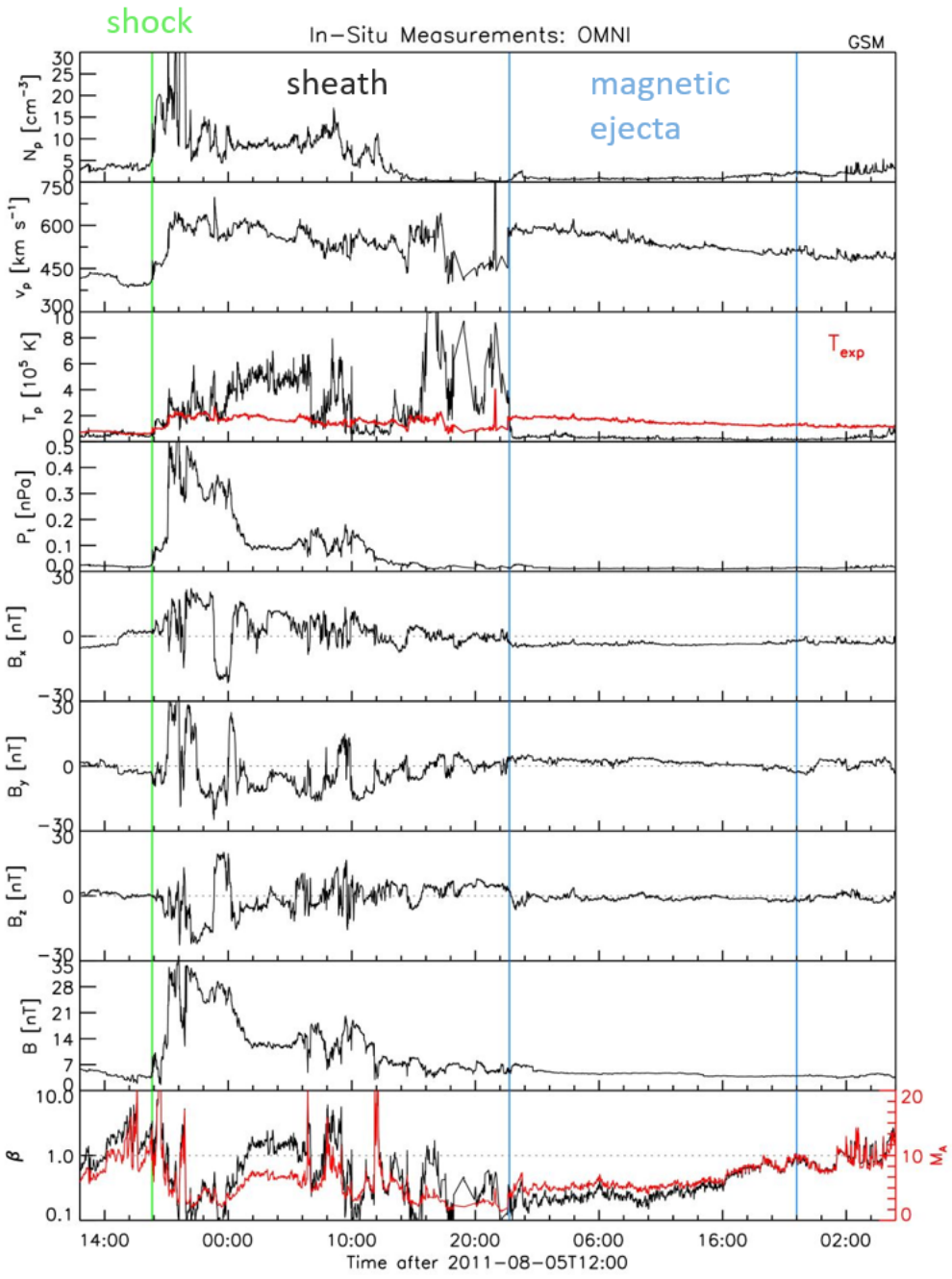

Figure 2.9: In-situ measured plasma parameters of the ICME from 4 August 2011 as extracted from NASA/GSFC's OMNI data set through OMNIWeb. This plot shows the proton number density N_p, the bulk velocity v_p, the proton temperature T_p with the expected proton temperature in case of normal solar wind expansion (Lopez, 1987), the total perpendicular pressure P_t (Russell et al., 2005), the components of the magnetic field in GSM (geocentric solar magnetospheric) coordinates (B_x, B_y, B_z), the total magnetic field B and the plasma β including the Alfvén Mach number M_A.

This shock is indicated as the green line in Figure 2.9. The shock is immediately followed by the sheath region which usually shows turbulent signatures in the defining parameters. The sheath region is followed by the *magnetic ejecta* or the *magnetic cloud* (MC Burlaga, 2002) depicted as the blue line in Figure 2.9). It is typically characterized by a smooth (low turbulence) and sometimes rotating magnetic field, low density and temperature, linearly decreasing velocity and low plasma β (Zurbuchen and Richardson, 2006). However, reality sometimes shows more complex structures. This can be the case if for instance multipe CMEs with different velocities gather in interplanetary space. Burlaga et al. (2002) call these events *complex ejecta*. An interesting correlation between the occurrence of MCs or complex ejecta and the solar activity was found by Cane and Richardson (2003). They associated about 60% MCs to solar minimum while at solar maximum they only found about 15% MCs with the rest being complex ejecta. This seems plausible in terms of multiply formed CMEs near solar maximum forming complex ejecta because of their interaction in interplanetary space. However, due to reasons of simplicity, we will only consider two parts within an ICME in-situ signature in the further course of this study. That is, the shock-sheath part which we will simply call *sh-sh* and the part of the actual CME flux rope which we will name *ME* (short for magnetic ejecta).

3 Spacecraft

Since the launch of the first spacecraft Sputnik 1 on the 4 October 1957 an immense number of objects departed from the Earth's surface to study the nature of outer space. For astronomers and their telescopes the main reason to do so is the advantage of no disturbing atmosphere between the object of interest and the lense that captures its light.

For the purpose of this study two separate sources of data were used. That is on the one hand spaceborne coronagraphs and on the other hand instruments that gather particle and plasma data. Those instruments have been parked at specific positions in the Sun-Earth system to fulfill their task. The following sections provide a list of the spacecraft and their instruments used in this thesis.

3.1 Solar and Heliospheric Observatory (SOHO)

As the result of a collaboration between the National Aeronautics and Space Administration (NASA) and the European Space Agency (ESA) they launched the *Solar and Heliospheric Observatory satellite* (SOHO) whereon the *Large Angle and Spectrometric Coronagraph* (LASCO; Brueckner et al., 1995) was installed. It has three coronagraphs called C2 and C3 differing mainly in the field of view (FOV). Taking white-light images from 3.7 to 30 solar radii the most important instrument for our purpose is the C3 coronagraph. Parked in a halo orbit around the Sun-Earth L1 point (Lagrangian point about 1.5 million km sunward in the Earth-Sun line; see Figure 3.1), LASCO provides images of the Sun ever since its launch on the 2nd December of 1995. Until the start of the STEREO mission at the end of 2006, LASCO was the only spaceborne coronagraph and therefore formed the base of many studies.

3.2 Solar Terrestrial Relations Observatory (STEREO)

On the 26 October 2006 the two probes STEREO A (Ahead) and STEREO B (Behind) were strapped upon a Delta II rocket and brought into their orbits. While STEREO A passed the escape velocity of the Earth - Moon - system

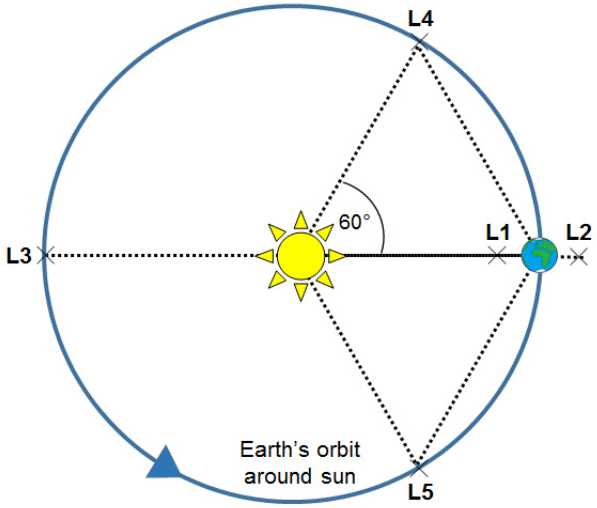

Figure 3.1: Representation of the Lagrangian Points in the Sun-Earth system.

with a lunar distance of 7322 kilometres and was ahead of the Earth in its orbit around the Sun, STEREO B was brought on an essentially higher transfer orbit and passed the Moon in a distance of 11750 kilometres. In an Earth - Sun fixed coordinate system, STEREO A and STEREO B move in opposite directions, so that a coverage of the Sun from different viewing angles was possible (see Figure 4.1). They separate approximately 44° per year seen from the Sun. Both probes have mounted two coronagraphs (COR 1 observing with a FOV of 1.5 - 4 $R_\odot$ and COR 2 with a FOV of 4 - 15 $R_\odot$) which are part of the *Sun Earth Connection Coronal and Heliospheric Investigation* instrument suite (SECCHI; Howard et al., 2008a) and an instrument for particle detection called IMPACT (In-situ Measurements of Particles and CME Transients). Thus, the two STEREO satellites provide us with both remote and in-situ data. Together with LASCO, the two coronagraphs of the STEREO probes provide a 3D view of the Sun and thus form the basis of our CME observation close to the Sun.

3.3 Advanced Composition Explorer (ACE)

Another satellite, managed by NASA, that measures particle flow is ACE. Reaching its destiny orbit close to L1 it has delivered data since the 21 January 1998. The two instruments important for this work are the magnetometer (MAG; Smith et al., 1998) and the *Solar Wind Electron, Proton, and Alpha Monitor* (SWEPAM; McComas et al. (1998)). MAG is a redundant triaxial flux-gate magnetometer providing information on the vector components of the magnetic field. SWEPAM was designed to measure characteristics of the solar wind. With its instrumentation it is not only able to measure the elemental and isotopic composition but also the 3D velocity, temperature and the proton

density of the surrounding plasma.

3.4 Wind

NASA launched the Wind satellite on the 1 November 1994 from the Cape Canaveral Air Force Station in Florida. As the name indicates it was designed to study the solar wind and thus represents one of the in-situ spacecraft used in this study. Especially density measurements from Wind are found to be more reliable compared to ACE (Skoug et al., 2004). Originally it was planned to put the spacecraft in an L1 orbit, but this was delayed due to the fact that SOHO and ACE were sent to the same location. Meanwhile Wind studied the magnetosphere and the near lunar environment. In May 2004 Wind has reached its destination point L1 and has contributed data to over 5000 scientific publications. Its instrumentation covers magnetic field information (Lepping et al., 1995) as well as plasma data (Kasper et al., 2002).

4 Method and data

The basic goal of this thesis is to compute the density of CMEs and its evolution in interplanetary space. Coronagraphs mounted on the spacecraft LASCO, STEREO A and STEREO B provide us with white-light images of the Sun which let us estimate the geometry and mass of CMEs. To reconstruct the geometry we apply the forward fitting model *Graduated Cylindrical Shell* (GCS; Thernisien et al., 2006, 2009) on these white-light images. Furthermore we obtain the mass (deprojected 3D) from combined STEREO A and B data. Via the simple relation:

$$n = m_{\mathrm{CME}}/V_{\mathrm{CME}} \tag{4.1}$$

one is able to calculate the density from those two parameters. From Bein et al. (2013) we know that a significant mass increase in the order of 2% to 6% can be found most prominently over the distance range of 10 $R_\odot$ - 15 $R_\odot$. At a distance of about 20 $R_\odot$ it can be assumed that the CME mass evolution ceases and a final mass is reached. This assumption modifies the equation above to:

$$n = m_{\mathrm{CME}}^{@20\mathrm{Rs}}/V_{\mathrm{CME}} \tag{4.2}$$

With the assumption of self-similar expansion of the CME geometry and a fixed mass one is now able to calculate the density propagation through interplanetary space. The results are compared to in-situ plasma flow measurements of the associated ICME taken by spacecraft at different locations in the solar system. Measured is the proton density in cm^{-3}. The shock-sheath (sh-sh) as well as the magnetic ejecta (ME) part of the ICME will be considered separately. As those two structures are generated by different physical processes, we may consider different scenarios for both the volume and the accumulated mass. As we will see, a trend towards piled up mass at the front of the ICME is highly likely.

In addition to the analysis that is performed as part of this thesis we will use data from established catalogues. Those are collections of parameters to specific CMEs and their ICME counterparts. The *Richardson & Cane* list (Richardson and Cane, 2010) provides data on near-earth ICMEs since 1996. It consists of information about ICME parameters based on in-situ signatures. To some of those ICMEs, the associated CME as seen from LASCO, is given. Another data source used in this work are the *HELCATS* (Heliospheric cataloguing) catalogues (https://www.helcats-fp7.eu/). As a third source of information we consider the *SHINE* list which consists of 29 events with information on the geometry as well as on the associated ICME signatures (Temmer et al., 2019 in preparation). These catalogues provide parameters from the GCS fitting also

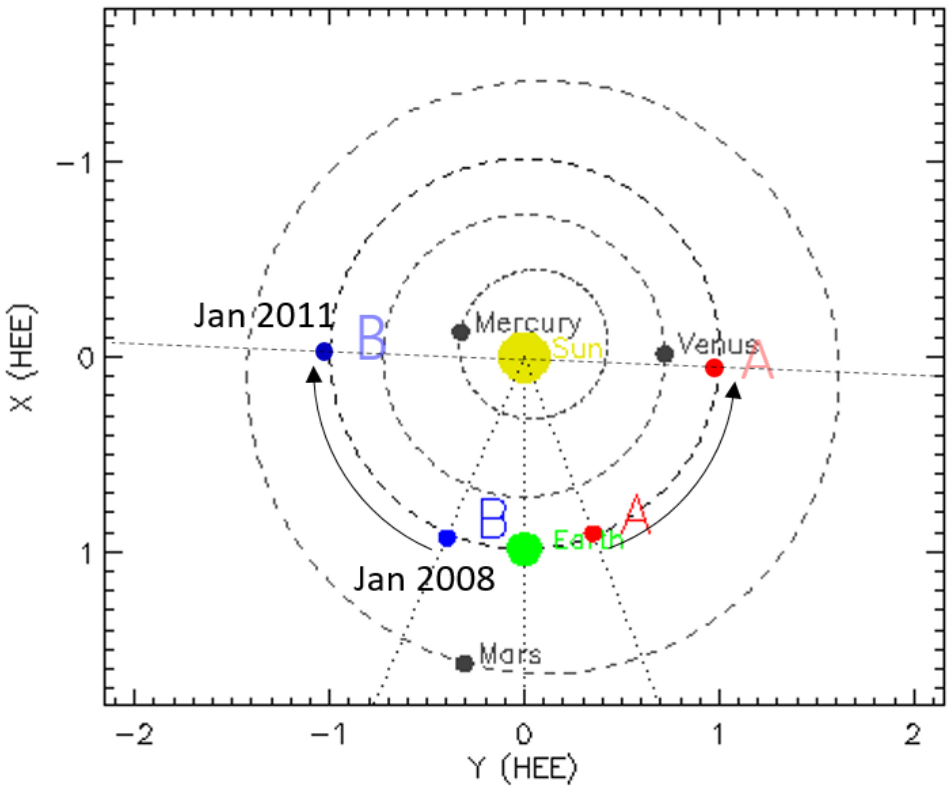

Figure 4.1: Location of the STEREO satellites in the HEE plane from January 2008 to January 2011. Adapted from https://stereo-ssc.nascom.nasa.gov/where.shtml

including mass and kinematical properties and some in-situ linked ICMEs.

All calculations and plots are computed with the programming language IDL (Interactive Data Language) and the statistical computing programme R (R Core Team, 2017). IDL is a data analysis tool especially designed for astronomy and geophysics. The white-light images of the STEREO spacecraft are stored on and accessed by an FTP server owned by NASA (https://stereoftp.nascom.nasa.gov/). The image data for the LASCO spacecraft is downloaded from the VSO (Virtual Solar observatory) which is funded by NASA. In-situ data are accessed by the *SolarSoft* system via ssc_get_winddata and get_ace_data.

4.1 CME 3D geometry and reconstruction

The downside of using only one coronagraph from e.g. SOHO (launched in 1995) is that the images are projected into the plane of sky. In fact, Howard et al. (2008b) showed that projected kinematical properties of CMEs can differ by a factor of up to 4.4 from a more sophisticated three dimensional measurement which was possible more than 10 years later after the launch of

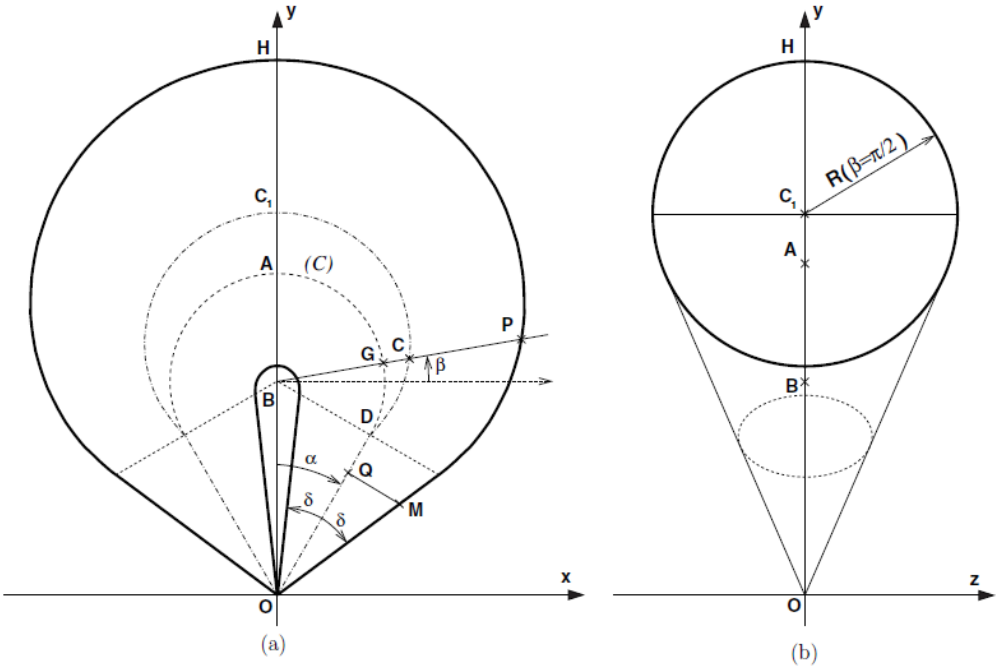

Figure 4.2: Sketch of the GCS model to reveal the structure from 2 different viewing angles. From Thernisien (2011)

STEREO. Hence, it is crucial to reconstruct CMEs using a 3D approach. The orbit locations of the two STEREO probes predefine the best time range for 3D observations of the Sun. Figure 4.1 shows the locations of STEREO A and STEREO B from January 2008 to January 2011. As the satellites separate approximately 22° per year with respect to the Sun-Earth line the optimal time span for 3D observations covers the years of late 2009 to early 2013. Due to the orbital periods this would not be the only time window for 3D observations but in October 2014 the contact to STEREO B was lost and could not be re-established. For an Earth-directed CME in the aforementioned time range one would have limb events for each of the two STEREO probes and a halo event seen on LASCO. Halo events, as seen in Figure 2.6, are characterized by a circle-like spread CME structure while limb events, as the name indicates, reveal the CME structure sideways.

4.1.1 The graduated cylindrical shell model

As mentioned earlier we reconstruct the geometry of CMEs with the GCS model. Ideally applied on both, the two STEREO and LASCO data at the same time, one is able to visualize the CME structure from three different viewpoints and therefore minimize projection effects. This model represents an idealized flux rope (Chen et al., 1997) which consists of two cones representing the legs of the CME and a torus-like structure connecting the legs. The structure as a whole is therefore often referred to as a croissant. It is well known that CMEs

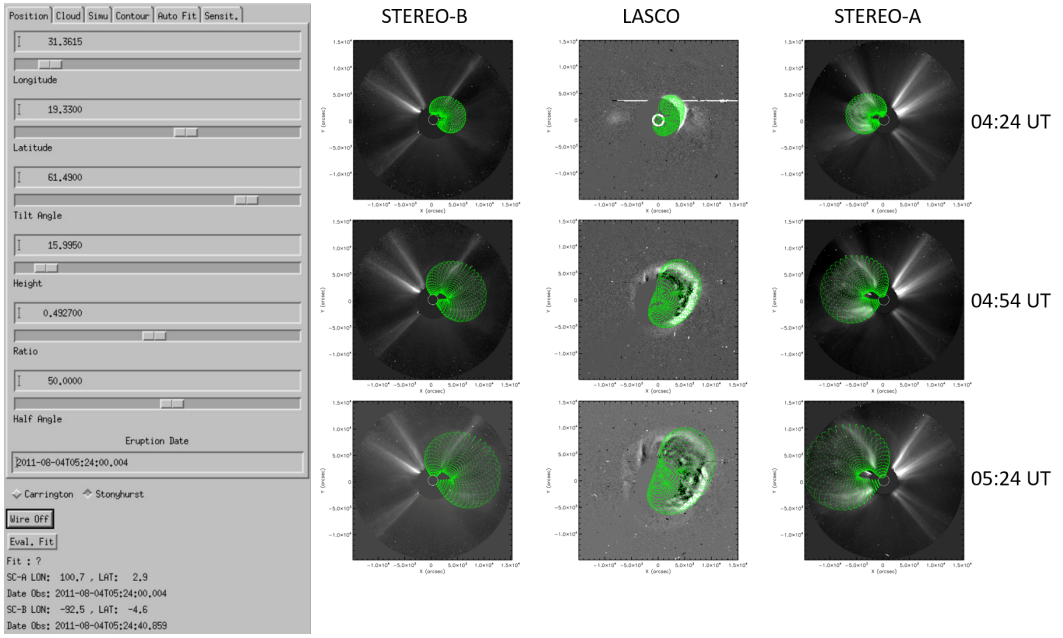

Figure 4.3: Screenshot of the graphical user interface in IDL with the resulting GCS reconstruction of the 4 August 2011 CME

tend to expand in a self-similar manner (see Chen et al., 2006, 2000, 1997). Combining these two characteristics in a unified model, the GCS has been used in numerous studies. In Figure 4.2 one can see a two-dimensional projection of the model with the most important angles, lengths and points that define the entire structure. All detailed equations and relations of the model can be found in Thernisien (2011).

In order to reconstruct CMEs with the GCS model we use a tool from *SolarSoft* providing a graphical user interface to apply the model to white-light images from STEREO A, B and LASCO. A snapshot of this GUI is shown in Figure 4.3. According to the visible shape of the CME one can adapt 6 parameters. The longitude and the latitude give information on the source region and direction the CME is heading to. These two parameters are taken from the HEE (Heliospheric Earth Ecliptic) plane. That is, we adjust to "Stonyhurst" in the settings. The latitude gives the north- or southward direction of the CME. The third parameter is called the CME's tilt angle. This parameter basically changes the positions of the footpoints, i.e., rotates the CME counterclockwise with respect to each other. For instance, a zero degree tilt corresponds to horizontally aligned footpoints, whereas 90 degrees tilt mean vertically aligned footpoints. The fourth parameter is the height of the leading edge defined as the distance of the CME apex from the solar surface. The last two parameters are directly related to the shape of the GCS. The aspect ratio κ is defined as the sine of δ which, see Figure 4.2, is the half-angle of the cones. This parameter is responsible for the self-similarity of the model, since it sets the rate of expansion against the height of the CME. The second important parameter concerning

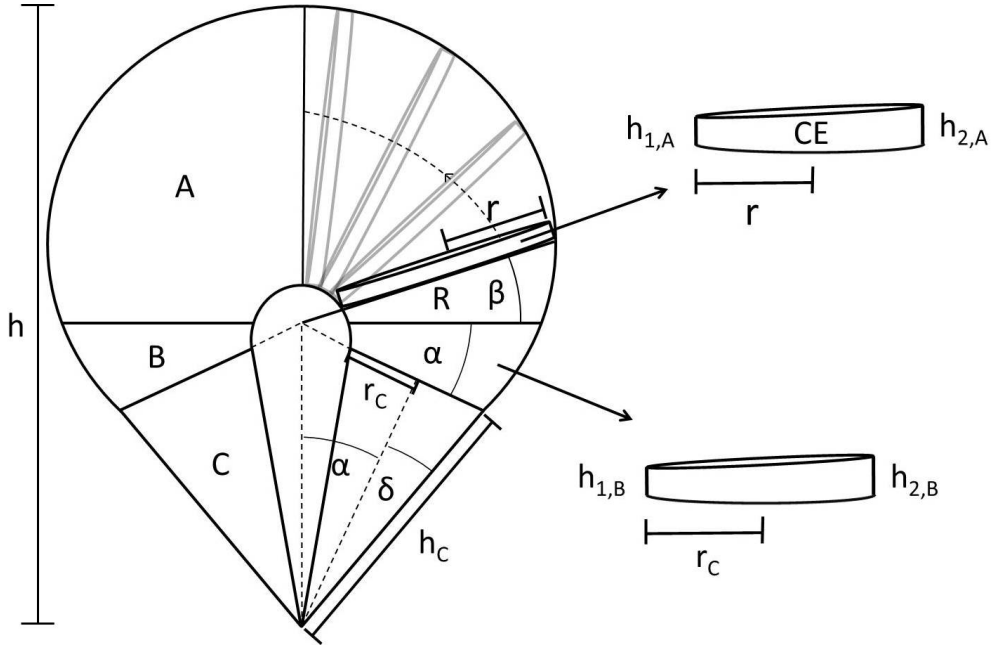

Figure 4.4: Illustration of the volume determination from the GCS reconstruction. Adapted from Holzknecht et al. (2018)

the shape of the CME is the half-angle α (see also Figure 4.2). It defines how far the two cones are separated from each other.
For simulating self-similar expansion the same set of parameters (longitude, latitude, tilt angle, aspect ratio κ, half-angle α) is used and only the height is adapted. It turns out, that the process to achieve the best reconstruction involves back and forth fitting. The parameters height, aspect ratio κ and half angle α entirely define the geometry and therefore the volume of the CME.

Volume

At a first glance on the two-dimensional structure of the GCS (see Figure 4.2) one might assume that it is easy to derive the volume of the GCS model, since it is simply half a torus strapped upon two cones. Taking a closer look though (applied GCS reconstruction Figure 4.3), reveals some significant problems with this assumption. In fact, the structure that connects the two cones differs drastically from a simple torus, as the inner radius (cross section radius r in Figure 4.4) is not a constant value, but changes within the structure. Additionally there remains a rest volume between the half-torus and the cones. It is certain that one can make simplified assumptions to get a rough estimation on the order of magnitude. Nevertheless, we aim to have a stable and easily comprehensible approximation working directly with the equations and parameters of the GCS model.

Our approach is to separate the entire structure into three different parts (A, B and C; see Figure 4.4). This separation may also be used to estimate the

density distribution within different parts of the CME separately. Volume C simply represents the volume of a cone with the height h_C and the radius r_C:

$$V_C = r_C^2 \pi \frac{h_C}{3} \tag{4.3}$$

For Volume A we extract a large number of small cylindrical elements (CEs). We sample these CEs from $\beta = 0°$ to 90° with a constant fraction (γ) of β. The value of γ hence depends on the amount of CEs one wants to compute. In our case we cut out 1000 CEs so that the value of γ is 0.09° ($\frac{90°}{1000}$). Note that each of these elements has two different heights. These heights can be calculated by the distance R and the cross section radius r as given by equations (19) and (27) in Thernisien (2011):

$$h_{1,A} = \tan(\gamma)(R - 2r) \tag{4.4}$$

$$h_{2,A} = \tan(\gamma)R \tag{4.5}$$

Calculating the volume of these elements and summing them up comprises volume A:

$$V_{CE} = r^2 \pi \frac{h_1 + h_2}{2} \tag{4.6}$$

$$V_A = \sum V_{CE} \tag{4.7}$$

Volume B is calculated by a similar approach, namely a CE that is cut between the upper end of the cone and the x-axis (corresponding to $\beta = 0$):

$$h_{1,B} = \sin(\alpha)(R - 2r[\beta = 0]) \tag{4.8}$$

$$h_{2,B} = \sin(\alpha)R[\beta = 0] \tag{4.9}$$

$$V_B = r_c^2 \pi \frac{h_{1,B} + h_{2,B}}{2} \tag{4.10}$$

As the structure is axisymmetric, the total volume V_{Total} of the GCS model is two times the sum of A, B, and C:

$$V_{Total} = 2(V_A + V_B + V_C) \tag{4.11}$$

The entire volume calculation requires only two GCS parameters, the half-angle α and the aspect ratio κ. Due to the fact, that the GCS reconstruction is done manually, there is no real consensus of the goodness of the fit. Hence, we estimate the error for the reconstruction via comparing GCS results done by various groups in terms of α and κ. The average difference of a sample of 9 events from the SHINE list predicts an error for α of about $\pm$ 0.15 rad and κ of about $\pm$ 0.10 rad. Assuming average values from 29 events from the SHINE list for $\alpha = 0.52$ rad and $\kappa = 0.41$ rad leads to a spread in the calculated volumes of $V_{215} = 7.8 \times 10^{24}$ km^3 $\pm$ 38%.

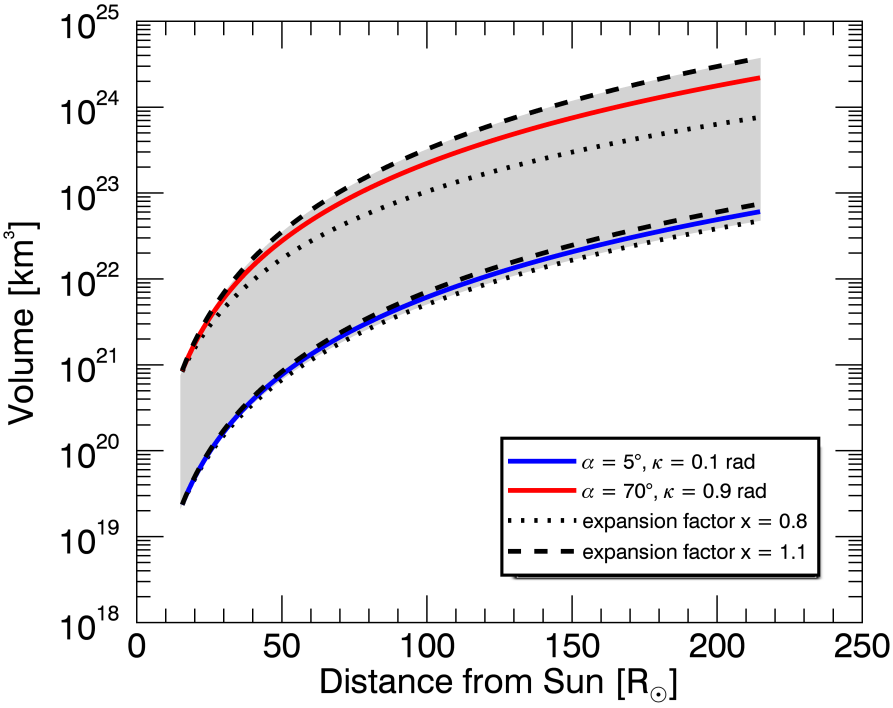

Figure 4.5: Volume distribution of the GCS model. The grey shaded area are displays the possible results for physically meaningful GCS parameters α and κ (note that κ is the sine of δ) with different expansion factors x. Adapted from Holzknecht et al. (2018).

Usually the model depicts self-similar expansion of the CME. However, we will also have a look at different expansion factors x for the CME radius:

$$R(r) = R(0) \left(\frac{h(r)}{h(0)} \right)^{\mathrm{x}} \tag{4.12}$$

with R referring to the cross section radius r see Figure 4.4, the distance r and the height of the CME h. Self-similar expansion is characterized by $x = 1$, but observational studies (Bothmer and Schwenn, 1998; Vršnak et al., 2019) showed that values around $x = 0.8$ to 1.1 might lead to results that resemble the actual CME expansion more accurately.

Figure 4.5 shows the computed volumes of the GCS reconstruction for a physically meaningful range of both the half-angle α and the sine of the half-angle of the cones δ. The ranges of α and κ are taken from the HELCATS GCS catalogue (https://www.helcats-fp7.eu/catalogues/wp3_kincat.html) covering 122 CMEs. They give values for α between 5° and 70° and for κ between 0.1 and 0.9. Additionally, as the dotted ($x = 0.8$) and dashed ($x = 1.1$) lines, we give the results from different expansion factors x for each of the two propagation lines.

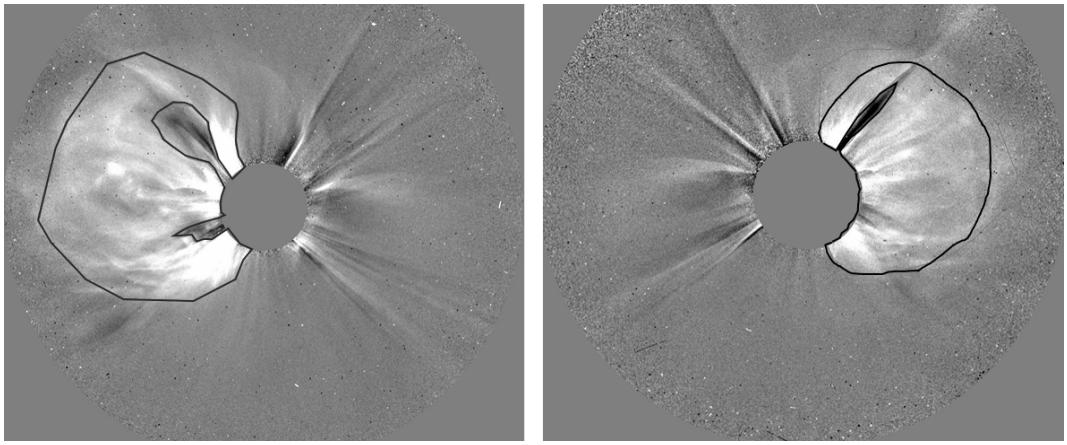

Figure 4.6: Mass images (left panel: STEREO A COR2, right panel: STEREO B COR2) of the 4 August 2011 CME at 05:08 UT. The brightness changes in the images are solely caused by the CME. The black parts are exempted from the 3D mass measurement since they would distort the calculation in terms of negative values.

4.1.2 Mass

As discussed in Chapter 2.3 the effect of Thomson scattering is the basis to obtain the mass of a CME from simple white-light images. In order to account for projection effects from the simple plane of sky (POS) by using for instance only one coronagraph (when LASCO was the only available instrument) we use a similar approach like in the aforementioned GCS reconstruction. Combining again images of the two STEREO probes we can use the angle dependence of the Thomson scattering geometry to get a more "realistic" de-projected 3D mass of a coronal mass ejection (Colaninno and Vourlidas, 2009). To only consider the excess mass of the CME, one needs to subtract the F- and K-corona by subtracting an image of the sun before the CME started to erupt. This method ensures that the excess brightness is entirely caused by the CME. With the assumption of a CME's material composition of 10% helium and 90% ionized hydrogen one can calculate the mass for each pixel of such a mass image via:

$$m = \frac{B_{\mathrm{obs}}}{B_{\mathrm{e}}(\theta)} \times 1.97 \times 10^{-24}[\mathrm{g}] \tag{4.13}$$

with the observed brightness B_{obs} and the analytically calculated brightness of a single electron at a certain angle $B_e(\theta)$ (Billings, 1966). Finally the total mass of the CME is calculated by summing up all the pixel values in the region of the CME. As already mentioned, we assume that at approximately 15-20 $R_\odot$ (which roughly corresponds to the FOV of STEREO A and B), the CME reaches its final mass (Bein et al., 2013). That is, the time of the CME mass image is often close to the time of the last GCS fit. We will call this the starting (excess) mass m_0 of the CME. While the straight forward calculation itself has a low noise level, the selection of what actually comprises the CME often depicts a source of an error. This can be led back to the fact, that in some

viewpoints streamers and similar structures can not be distinguished from the CME (Colaninno and Vourlidas, 2009).

4.1.3 Density

With the assumptions of a constant mass m_0 within the CME and its expanding volume one is now able to compute the CME's density evolution in interplanetary space. It is important to note that we expect to measure this density for the associated ICME with in-situ data. However, it has to be stressed, that this density is only valid for the magnetic ejecta (ME) part of the ICME. For the shock-sheath (sh-sh) part we expect a mass pile up from the ambient solar wind. In fact, DeForest et al. (2013) found that the CME mass increases by a factor of 1.6 during its journey in interplanetary space.

With typical excess masses m_0 ranging from 10^{14} to 10^{16} g and the accompanying volumes V of 10^{19} km^3 to 10^{21} km^3 at approximately 15 R$_\odot$ one easily derives densities of 10^{-18} to 10^{-16} kg m^{-3}.

To derive the expected in-situ density of the associated ICME we expand the CME's volume to a distance of 215 R$_\odot$ (V_{215}) and obtain volume ranges of 10^{22} to 10^{24} km^3. In order to be able to compare the calculated densities with the measured ones, we convert the measures of kg m^{-3} to the proton number density via:

$$n_\mathrm{p} = \frac{m_0}{(V_{215} m_\mathrm{p} 10^{15})} \tag{4.14}$$

with the proton mass $m_\mathrm{p} = 1.673 \times 10^{-24}$g. The conversion factor 10^{15} has to be applied because V is given in km^3 whereas the in-situ proton density is measured in cm^{-3}.

The resulting calculated proton densities for the ME region at 215 R$_\odot$ stem from approximately 1.0 to 30 cm^{-3}. As a first check we compare the results with in-situ measurements from the HELCATS WP4 catalogue (https://www.helcats-fp7.eu/catalogues/wp4_icmecat.html). Containing 668 ICME encounters with 125 Earth-directed (measured by the Wind spacecraft; thus we will call this catalogue *HELCATS Wind*) events from 2007 to 2015 (cf. Table .1 in the Appendix) it reveals ME density values ranging from 1.1 $\pm$ 0.2 cm^{-3} to 26 $\pm$ 17 cm^{-3} with an average value of 7.4 $\pm$ 4.7 cm^{-3} (errors refer to the standard deviation).

However, Equation 4.14 is a rather simplistic approach assuming the volume to be V_{215}. Later in this thesis we will introduce a more sophisticated approach to estimate the volume of the ICME structure (see Chapter 4.2) in order to derive the ME density differently. We will nevertheless use the simplistic approach to derive the density of the ME region and call it dens_me1.

We assume m_0 to be equally distributed within the ME region of the ICME (i.e. to the flux rope part of the CME) and that there is no mass exchange

with the heliosphere in this region. But as the sh-sh region represents a part of the ICME where solar wind material can be piled up in front of it, we usually measure much higher densities within this part.

For the same set of events as given from the *HELCATS Wind* catalogue for the ME region, the sh-sh densities vary from 1.1 ± 0.1 cm^{-3} to 45.9 ± 21.5 cm^{-3} with a mean value of 11.9 ± 6.8 cm^{-3}.

In order to account for these high densities one has to switch to a different approach. An opportunity to obtain the piled up mass is to simply follow the average mass increase found by DeForest et al. (2013) and multiply the excess mass by a factor of 1.6. This yields for the sh-sh mass $m_{sh-sh} = 1.6 \times m_0$. Our aforementioned assumption, based on the fact that the initial mass stays constant, requires a different interpretation. The most plausible approach is to imagine the CME as a kind of bulldozer sweeping up the mass of the interplanetary medium (i.e. the solar wind) in front of it. This mechanism is closely related to the already mentioned aerodynamic drag model (see Chapter 2.3.1) and the *snow plough* model (Cargill, 2004; Tappin, 2006; Vršnak et al., 2013) which leads us to the aforementioned (Equation 2.8) *virtual mass*.

4.1.4 Virtual mass

The concept of the *virtual mass* was introduced by Batchelor (2000) and Cargill et al. (1996). It represents an input parameter within the aerodynamic drag model as stated in Equation 2.8 and accounts for the material of the solar wind that can be piled up by the ICME in interplanetary space. Hence, it is an important parameter for the mass development of the ICME. According to Batchelor (2000) and Cargill et al. (1996) the virtual mass is defined as:

$$MV_{\mathrm{Cargill}} = \frac{\rho_{\mathrm{SW}} V_{\mathrm{ICME}}}{2} \tag{4.15}$$

with the solar wind number density ρ_{SW} and the ICME volume V_{ICME}. For the solar wind density we furthermore consider the model from Leblanc et al. (1998) which gives the SW density as a function of distance as:

$$\rho_{\mathrm{SW}}(r) = \frac{N}{7.2} \times 3.3 \cdot 10^5 \times r^{-2} + 4.1 \cdot 10^6 \times r^{-4} + 8.0 \cdot 10^7 \times r^{-6} \tag{4.16}$$

with the normalization variable N giving the ambient solar wind density before the arrival of the ICME shock front. N usually lies in the range between 4 and 8 cm^{-3}. However, Equation 4.15 simply assumes that the material can be piled up within half the total volume of the ICME. Which might or might not be a reasonable assumption.

Therefore, we will also consider a different method for computing the volume fraction of the ICME that piles up the SW mass in front of it (see Figure 4.7). This method subsequently subtracts a smaller CME from a larger one (height

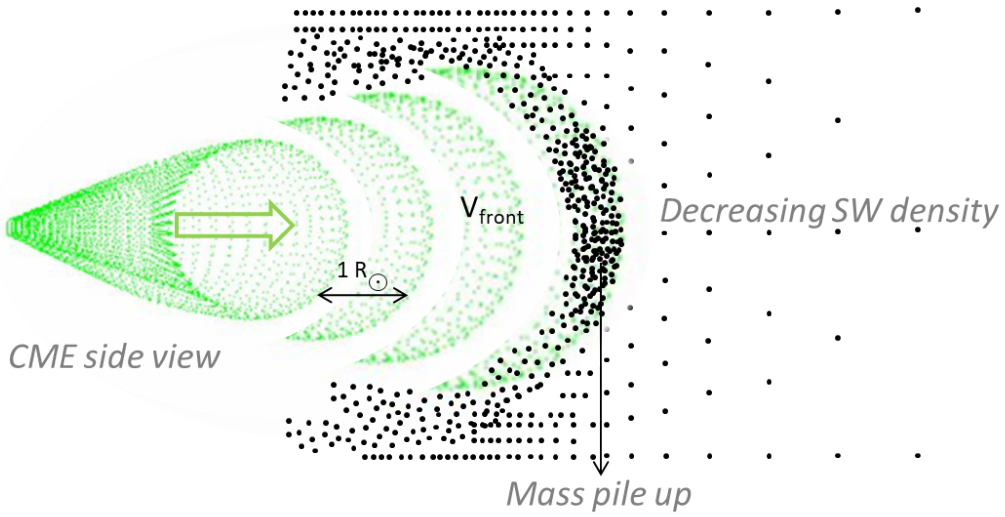

Figure 4.7: Graphical representation of the mass pile up in interplanetary space. The CME's geometrical representation from the GCS model is shown sideways. To illustrate the propagation and also the method explained via Equation 4.17 we give four images of the CME, where each one has a leading edge that is 1 $R_\odot$ larger than the previous.

difference between the two: 1 $R_\odot$). Note that we only take the frontal shell part of the total CME ($V_{\text{front}} = 2 \times Vol(A)$ according to Figure 4.4). Computing

$$MV_{\text{shell}}(r) = \rho_{\text{SW}}(r)\,[V_{\text{front}}(r) - V_{\text{front}}(r-1)] \tag{4.17}$$

in steps of $r = 1$ $R_\odot$ and summing up all values up to 215 $R_\odot$ will give the total mass that the ICME is able to pile up in interplanetary space. Assuming values for the volume showed in Figure 4.5 and applying Equation 4.17 leads to values of the piled up mass in the range of 2.3×10^{14} g to 9.7×10^{16} g. However, this method depicts an upper limit of the real mass pile up since there will always be a mass loss at the sides of the CME as it plows through interplanetary space (very much like a *wedge plow*; see also Figure 4.7). We will account for this loss by fractioning MV_{shell} as a function of the CME's half angle α. We assume that the larger α (as a fraction of the maximum value of 90°) is, the more mass will be taken along with the CME and thus the mass loss at the sides of the CME will be less. Equation 4.17 thus transforms into:

$$MV_{\text{shell}}(r) = [\rho_{\text{SW}}(r)(V_{\text{front}}(r) - V_{\text{front}}(r-1))]\frac{\alpha[^\circ]}{90} \tag{4.18}$$

Another rather simple approach is to consider conservation of momentum to account for the additional mass input in the sh-sh part of the ICME. Knowing the initial speed v_0 and mass m_0 of the CME and the average velocity of the ICME in the sh-sh part $v_{\text{sh-sh}}$ we can estimate the virtual mass directly from measurements. Conservation of momentum requires:

$$m_0 v_0 = (m_0 + MV_{\text{conservation}})v_{\text{sh-sh}} \tag{4.19}$$

Hence, the piled up mass is calculated by:

$$MV_{\text{conservation}} = \frac{m_0 v_0}{v_{\text{sh-sh}}} - m_0 \tag{4.20}$$

For simplification reasons we will rename these parameters from MV_{shell}, MV_{Cargill} and $MV_{\text{conservation}}$ to MV1, MV2 and MV3 respectively.

4.2 Connecting CMEs to ICMEs

In order to compare remote sensing and in-situ measurements, we need to unambigously connect CMEs and ICMEs. As stated in Chapter 2.3.1 this is not always a straightforward task. Nevertheless, the GCS reconstruction provides information about the CME's size (GCS parameter height) and with the time at each fit of the evolving CME we can quite accurately measure the initial speed v_0 within STEREO's COR2's FOV (i.e. 15 $R_\odot$). With that, one can use propagation models, such as the drag-based model (DBM; Vršnak et al., 2013), to estimate an arrival time at 1 AU and search for in-situ ICME signatures in the measurements or catalogues. An online platform to interactively use this model is offered by the University of Zagreb http://oh.geof.unizg.hr/DBM/dbm.php and ESA service http://swe.uni-graz.at/. The DBM uses an analytical solution of Equation 2.7 as it assumes a few simplifications. These include that beyond 20 $R_\odot$ the following approximations are valid: $A \propto r^2$, $\rho_{\text{SW}} \propto r^{-2}$, $M = const.$, $c_{\text{d}} = const.$ and $M \gg M_{\text{V}}$ (ibid.). Thus, one gets $\gamma(r) = const.$ and assuming a constant solar wind velocity v_{SW} leads to a solution of Equation 2.7 for the velocity:

$$v(t) = \frac{v_0 - v_{\text{SW}}}{1 \pm \gamma(v_0 - v_{\text{SW}})t} + v_{\text{SW}} \tag{4.21}$$

and for the distance:

$$r(t) = \pm\frac{1}{\gamma} ln[1 \pm \gamma(v_0 - v_{\text{SW}})t] + v_{\text{SW}}t + r_0. \tag{4.22}$$

The $\pm$ indicates whether the initial CME speed v_0 is greater (+) or smaller (−) than the surrounding solar wind speed v_{SW}. As an example we give the estimation for the arrival of the ICME associated with the CME erupting from the Sun on the 4 August 2011. The result of the DBM with the input parameters given in Table 4.1 is as follows:

- CME arrival at target (1 AU) [date and time]: 5 August 2011 23h:06
- Transit time: 41.71 h
- Impact speed at target (at 1 AU): 653 km/s

With the outcome of the DBM one is now able to look for the associated ICME signatures in the measurements in a limited time window. For our example CME we find the corresponding ICME shock at 18:00 UTC and the ME region

Table 4.1: Example of input parameters for the DBM.

CME start date [yyyymmdd]	20110804
CME start time [UTC]	05:24
r_0 ... starting radial distance of CME [$R_\odot$]	16.5
v_0 ... speed of CME at r_0 [km s^{-1}]	1700
γ ... drag parameter [10^{-7} km^{-1}]	0.2
v_{SW} ... ambient solar wind velocity [km s^{-1}]	387

at approximately 22:00 UTC on the 5 August 2011 (see Figure 2.9). The impact speed for the ME region is about 600 km s^{-1}. These values are in accordance to the predicted results from the DBM.

4.2.1 ICME assigned geometry and density

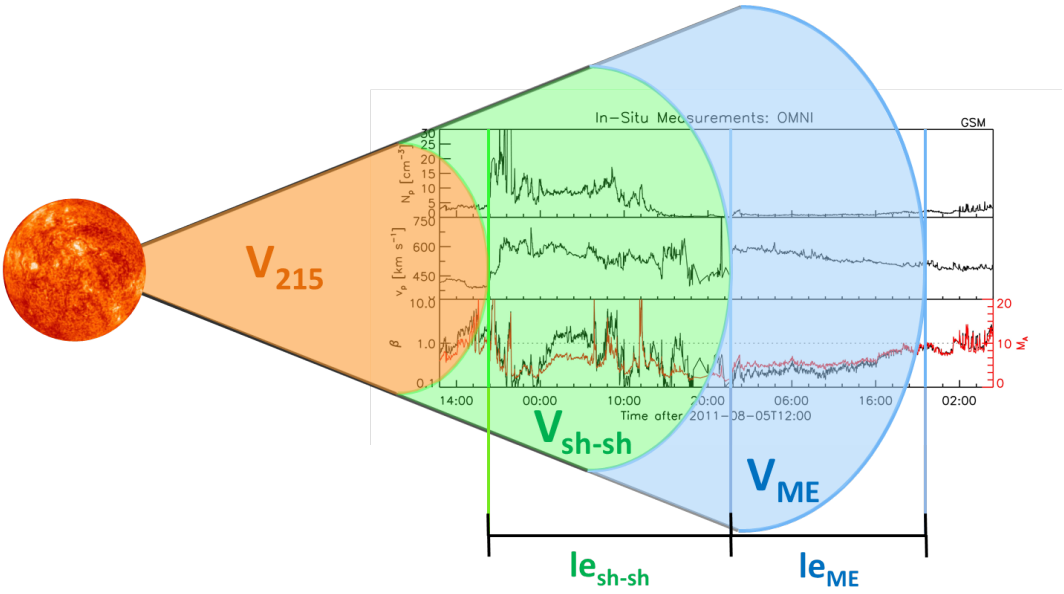

Figure 4.8: This sketch graphically demonstrates the different ICME volumes. The green line marks the start of the sh-sh region and the blue lines are the borders of the ME region. The volumes of the ICME regions are then calculated according to Equations 4.23 and 4.24.

We need to distinguish between two different parts of the CME in order to compare the remotely calculated density with actual in-situ measurements. That is on the one hand the ME region with its associated *excess* mass m_0 and on the other hand the sh-sh region with the associated *pile-up* mass. Having calculated these two masses one now needs to assign the associated volume to each region. In the previous approach to get a first estimate on the density range for the ME region (see Chapter 4.1.3) we simply take the CME volume at

215 $R_\odot$. A more realistic scenario however is to include more details from in-situ measurements. Since we assign both, the ME and the sh-sh region with a start and end time we can use additional information about the CME properties. Hence, we can assign a length to the regions by multiplying the average speed with the duration of each region. Subsequently, the calculated length should be representative of the CME length for both regions. We get the length of the ME and the sh-sh region and call them le_{ME} and $le_{\mathrm{sh-sh}}$ respectively (see Figure 4.8). The *HELCATS Wind* catalogue reveals average lengths of about 20.2 ± 15.8 $R_\odot$ for the sh-sh and about 43.6 ± 25.8 $R_\odot$ for the ME region. To compute the volume taking into account the spatial extension in a reasonable way we take the following approach:

$$V_{\mathrm{ME}} = V_{215+\mathrm{le}_{\mathrm{sh-sh}}+\mathrm{le}_{\mathrm{ME}}} - V_{215+le_{\mathrm{sh-sh}}} \tag{4.23}$$

$$V_{\mathrm{sh-sh}} = V_{215+\mathrm{le}_{\mathrm{sh-sh}}} - V_{215} \tag{4.24}$$

A picturesque representation for a better understanding of these equations is given in Figure 4.8. With the volume profile for different distances (as given in Figure 4.5) and the average lengths of both regions Equation 4.23 and 4.24 lead to a volume range between 1.9×10^{22} km^3 and 1.6×10^{24} km^3 for the ME region and between 1.6×10^{21} km^3 and 1.0×10^{24} km^3 for the sh-sh region. Hence one is now able to calculate the expected densities in each of the two ICME regions. With a typical excess mass (m_0) of about 5×10^{15} g and an average sized CME ($\overline{\alpha} = 0.52$ rad, $\overline{\kappa} = 0.41$ rad) with an average length ($\overline{le}_{\mathrm{ME}}$) of 44 $R_\odot$ one derives a density of about 4.4 cm^{-3} for the ME region. The thus derived ME density is called dens_me2 in the further course. For the sh-sh region we consider the piled up mass MV1 as described in Chapter 4.1.4 and Equation 4.18 and the sh-sh volume $V_{\mathrm{sh-sh}}$. Considering an average value for $MV1$ of about 7×10^{15} g and an average length ($\overline{le}_{\mathrm{sh-sh}}$) of about 20 $R_\odot$ we get a density dens_MV1 of 20.8 cm^{-3}.

5 Results and discussion

In this chapter we analyse multiple CME-ICME pairs. We will split this chapter into two parts. That is on the one hand a study on the correlations between the density and other plasma and magnetic field parameters measured by the in-situ spacecraft *Wind* within ICME regions. On the other hand we will put our density deriving methods as explained in Chapter 4 for both ICME regions to the test.

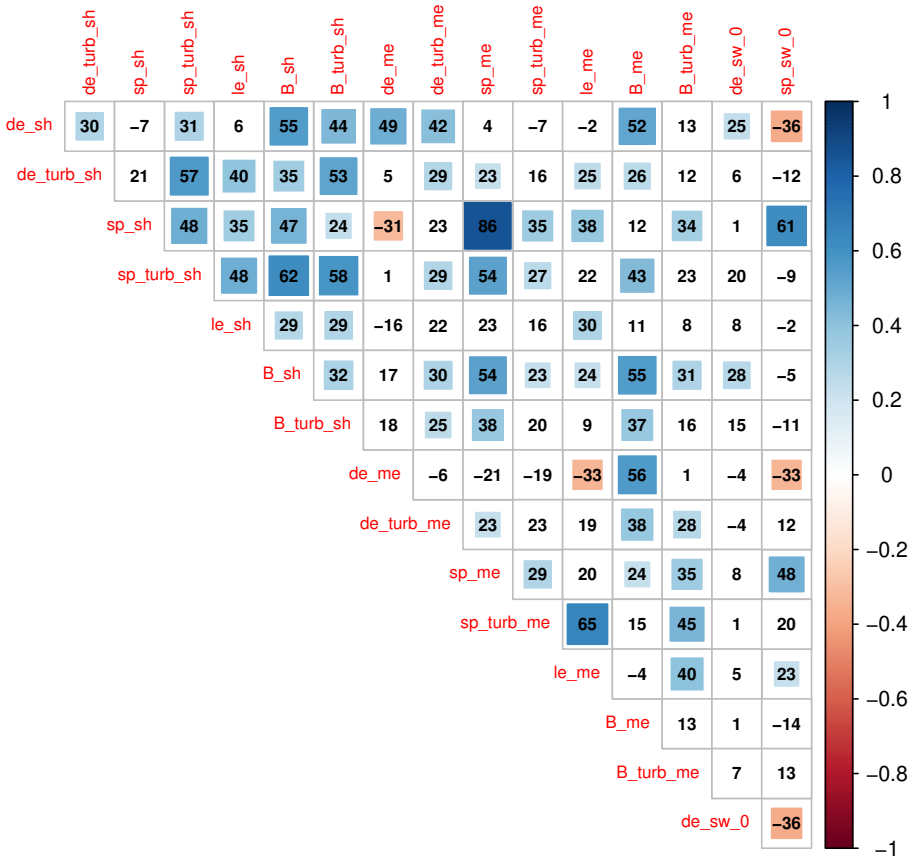

Figure 5.1: Correlation Matrix of the *HELCATS Wind* ICMEs. The value in the cells represents the percentage of the Pearson correlation coefficient. Correlations with p-values above 0.01 are considered as insignificant and are not color coded.

5.1 ICME in-situ parameters

We will start with the study of the in-situ parameters. For this we extract the start and end time of both the sh-sh and the ME region from the aforementioned *HELCATS Wind* catalogue containing 125 ICMEs (see Table .1 in the Appendix). For the assigned timestamps we analyse plasma and magnetic field data from the spacecraft. Note that the catalogue only provides in-situ observations and does not assign the according CMEs as observed remotely. The parameters under study are the density (de [cm^{-3}]), the speed (sp [km s^{-1}]), the length (le [$R_\odot$]) and the total magnetic field (B [nT]) averaged over each region (_sh for the sh-sh region; _me for the ME region). In addition to that, we give the turbulence intensity (_turb) of each parameter (obtained from the ratio of the standard deviation and the average value). Furthermore, we consider the density and the speed of the ambient solar wind (_sw) averaged over 36 hours before the arrival of the shock. Figure 5.1 shows the correlation matrix of all of the parameters. This matrix provides an important tool to delimit interesting linear correlations. However, the opposing behaviour of the parameters can be studied in more detail looking at scatterplots. Such plots are given in Figures 5.3 to 5.4. For each plot we give the Pearson correlation coefficient (R) and the p-value (p). The p-value gives information on the significance level of a sample. Values smaller than e.g. 0.01 are considered significant on a 99% level. Additionally we give the confidence interval (grey shaded area). Corresponding values can be found in the correlation matrix (see Figure 5.1).

In Figure 5.2 we present the measured results of all parameters for both ICME regions (ME region in golden color; sh-sh region in blue color). The average value for the sh-sh density is about 12 $\pm$ 7 cm^{-3} while it is 7 $\pm$ 5 cm^{-3} for the density in the ME region (see Figure 5.2a). Due to the linear decreasing velocity in the ME region we get slightly lower average speeds in this region (419 $\pm$ 85 km s^{-1}) compared to the sh-sh region (424 $\pm$ 91 km s^{-1}; see Figure 5.2b). The measured total magnetic field reveals average values for the sh-sh region of 8 $\pm$ 4 nT while the ME region shows slightly higher values of about 10 $\pm$ 5 nT (see Figure 5.2c). For the length it is found that the ME region with 46 $\pm$ 27 $R_\odot$ is on average larger than that of the sh-sh region with about 19 $\pm$ 16 $R_\odot$ (see Figure 5.2d).

Figure 5.3a and 5.3b show that the average density in the sh-sh region of the ICME is positively correlated with both the magnetic field and its turbulence intensity. Also, we determine correlations between the sh-sh and the ME density (rather weak) and its turbulence intensity (see Figure 5.3c and 5.3d). The increase in turbulence intensity of the sh-sh density is accompanied with turbulence in the sh-sh magnetic field (see Figure 5.3e).

Besides being correlated to the sh-sh density (see Figure 5.3c), the ME density shows the strongest correlation to the accompanying magnetic field (see Figure 5.4).

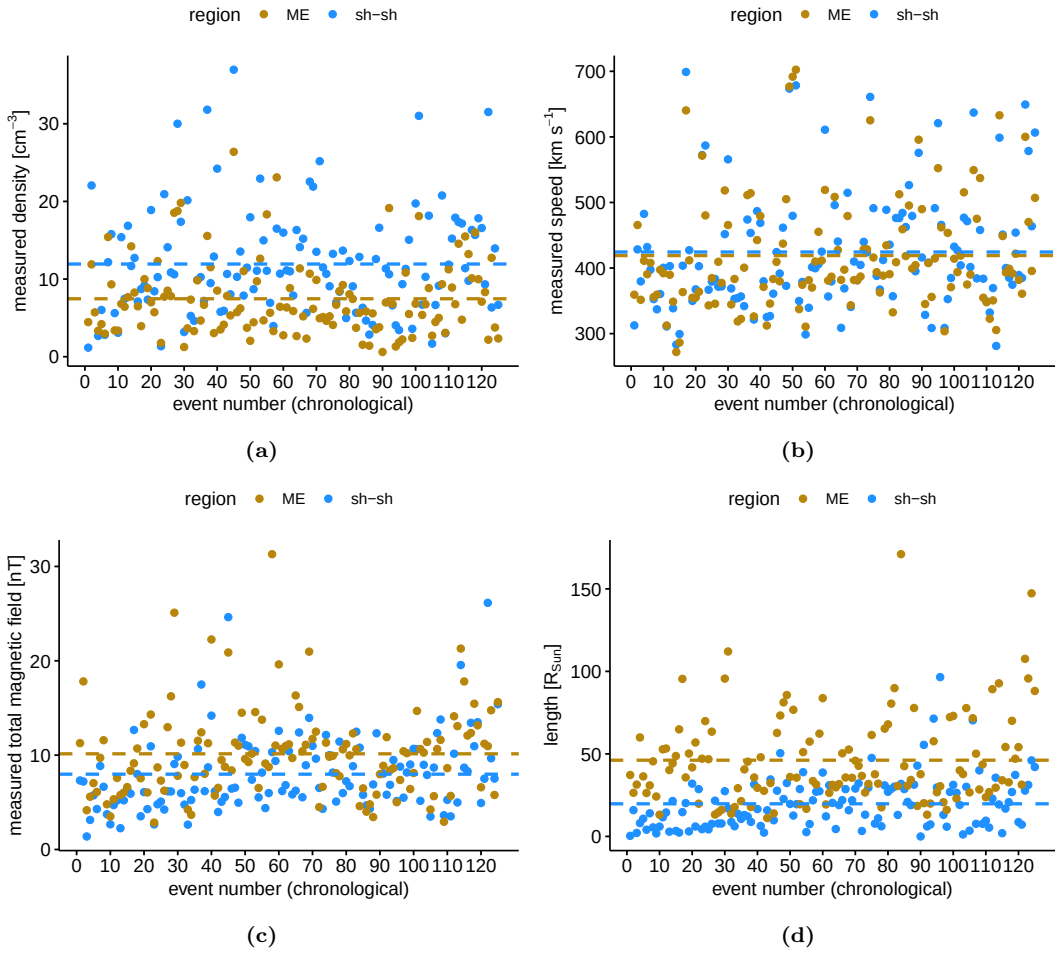

Figure 5.2: Comparison between average values for different in-situ measured parameters.

The magnetic field and its turbulence intensity demonstrate positive correlations especially with the sh-sh speed turbulence intensity and less with the average speed in this region (see Figure 5.5a and 5.5b). However, the exact opposite case holds true for the ME region (see Figure 5.5c and 5.5d), although the correlations in this region are very weak anyway. One additionally finds a correlation between the sh-sh and the ME magnetic field with R = 0.55 (see Figure 5.1). Generally, the speed and magnetic field correlation might hint towards the relation to the initiation process.

In Figure 5.6 we give speed related correlations for both regions. An interesting correlation can be found between the turbulence intensity of the ME speed and the length of the ME region (Figure 5.6c). An explanation might be that larger ME regions are accompanied by stronger magnetic pressure inside. Hence the CME might expand faster and with that reveals higher speed turbulence. A weak correlation of R = 0.45 is found according to Figure 5.6d. Comparing the correlation between the ME speed and the ME magnetic field turbulence intensity with the sh-sh region one obtains a difference in R of 0.26. This difference could be representative for the different mechanisms working in both

regions. An unsurprising correlation can be found between the sh-sh speed and the ambient solar wind speed. An explanation for this could be the adjustment of the CME speed with the ambient solar wind speed due to the drag force.

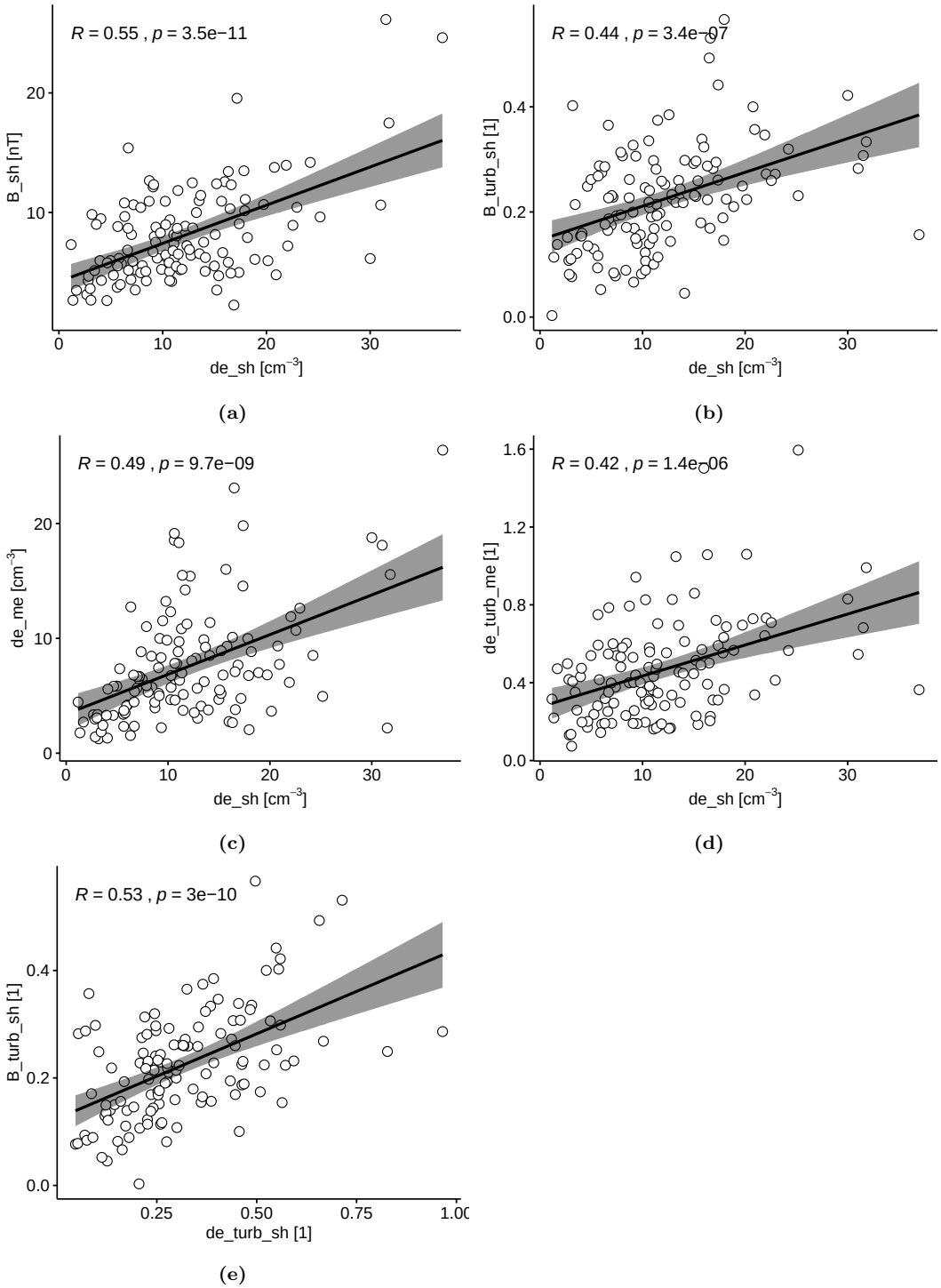

Figure 5.3: Correlations between the sh-sh density and other parameters. Upper panel: Correlation to the sh-sh magnetic field and its turbulence intensity. Middle panel: Correlation to the ME density and its turbulence intensity. Lower panel left: Correlation of the sh-sh density turbulence intensity and the sh-sh magnetic field turbulence intensity.

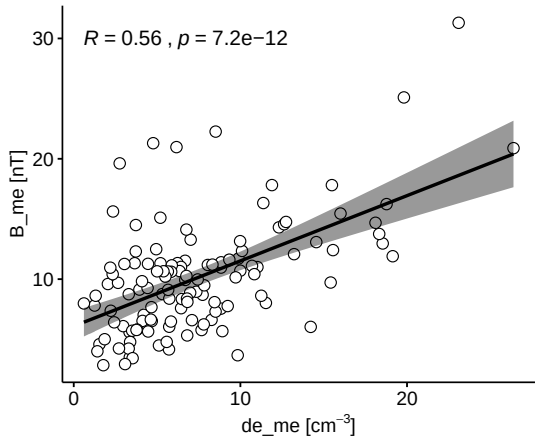

Figure 5.4: Correlation of the ME density and the ME magnetic field.

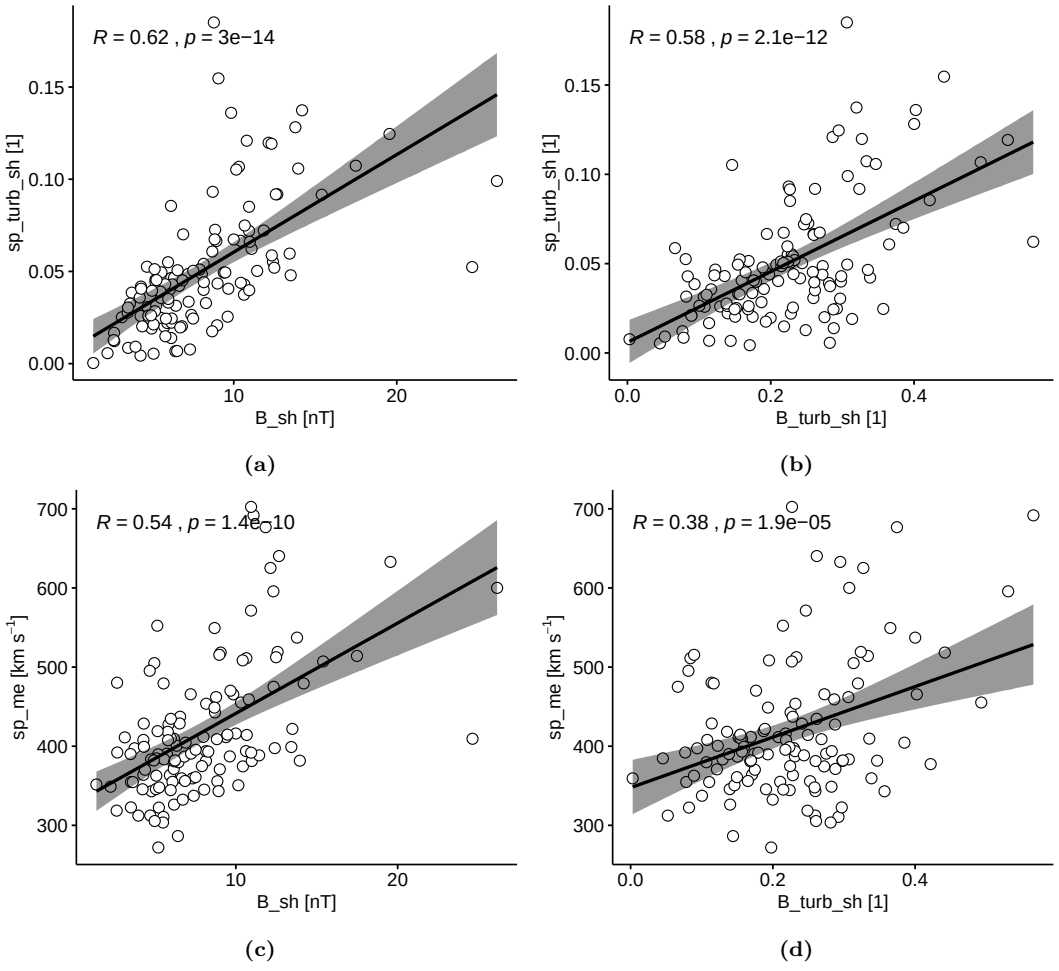

Figure 5.5: Upper panel: Correlation between the sh-sh magnetic field, its turbulence intensity and the sh-sh speed turbulence intensity. Lower panel: Correlation between the sh-sh magnetic field, its turbulence intensity and the ME speed.

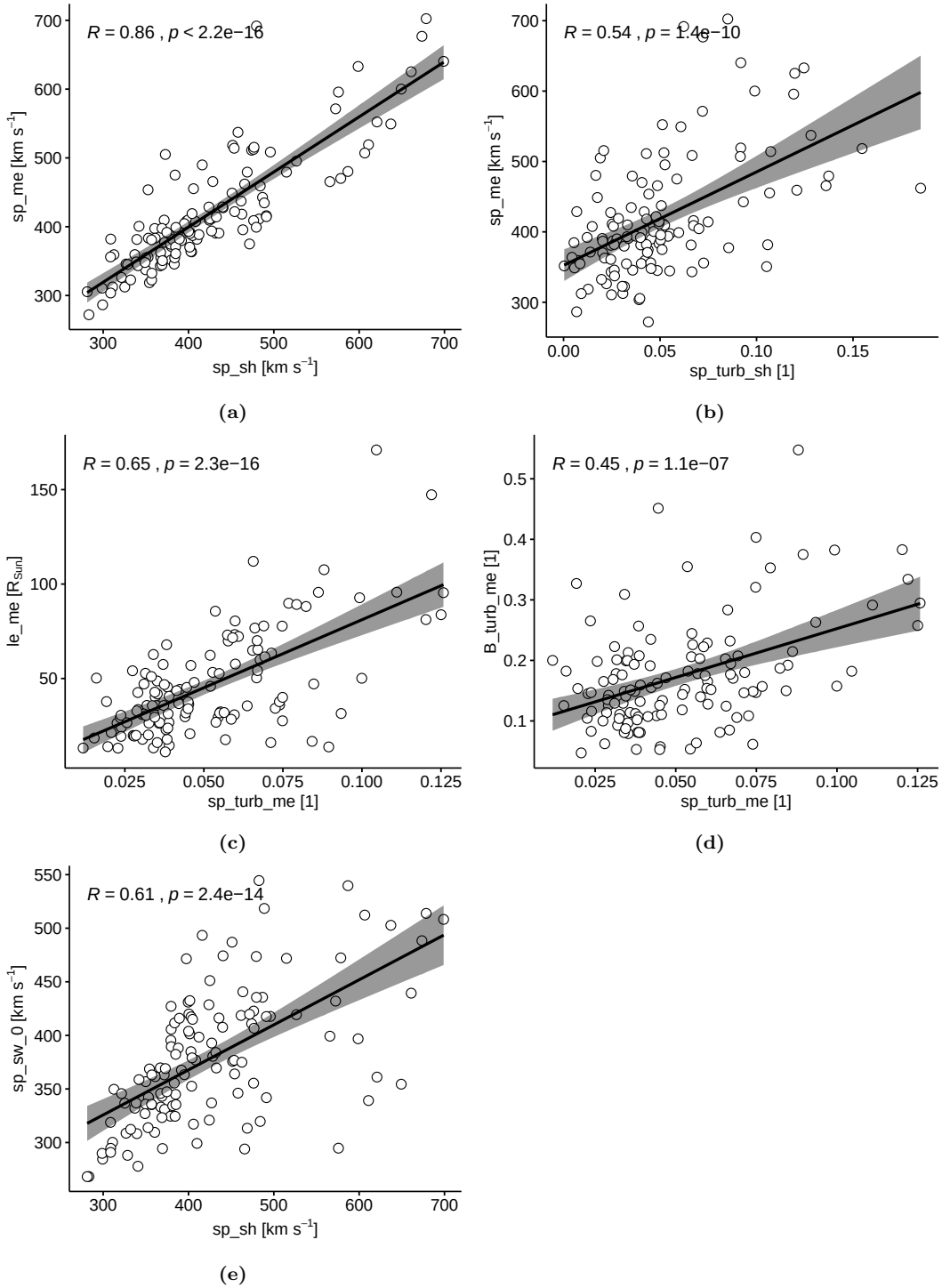

Figure 5.6: Upper panel: Correlation between the sh-sh speed, its turbulence intensity and the ME speed. Middle panel left: Correlation between the ME speed turbulence intensity and the ME length. Middle panel right: Correlation between the ME speed turbulence intensity and the ME magnetic field turbulence intensity. Lower panel: Correlation between the sh-sh speed and the ambient solar wind speed.

5.2 Derived CME vs. measured ICME density

For the comparison of remotely derived and in-situ measured densities we analyse a sample of 29 thoroughly studied events from the SHINE list (see Table .2). This CME-ICME event list combines remotely derived parameters (α [rad], κ [rad] (see Chapter 4.1.1), m_0 $\equiv m_0$ [g] (see Chapter 4.1.2), sp_0 $\equiv v_0$ [km s^{-1}] (see Chapter 4.2)), in-situ measured parameters (same nomenclature as in the previous section) and the following calculated values:

- The derived volume at 215 R$_\odot$ V_215 $\equiv V_{215}$ [km^3].
- For the density of the ME region we give two values. On the one hand the simplistic approach as already shown in Chapter 4.1.3 and Equation 4.14 dens_me1 $= m\_0/(V\_215 \cdot m_\mathrm{p} \cdot 10^{15})$. On the other hand we consider the reduced ICME volume assigned for the ME region (V_ME) as presented in Chapter 4.2.1 to compute the ME density dens_me2 $= m\_0/(V_\mathrm{ME} \cdot m_\mathrm{p} \cdot 10^{15})$.
- The virtual mass is calculated by three methods (MV1, MV2, MV3) as explained in Chapter 4.1.4.
- The according sh-sh densities as calculated by MV / $(V_\mathrm{sh-sh} \cdot m_\mathrm{p} \cdot 10^{15})$ are called dens_MV1, dens_MV2 and dens_MV3 respectively.

The start and end time of the sh-sh and the ME regions are taken from the *Richardson & Cane* list. In Figure 5.7 we present the correlation matrix for all parameters as given in Table .2 (see Appendix). A more extensive correlation matrix is given in the Appendix. It also includes results for the calculated values applying different volume expansion factors (0.8, 0.9, 1.1; called _ex08, _ex09, _ex11 respectively). Values with expansion factor 1 have no additional shortcuts (e.g. V_215 represents the volume at 215 R$_\odot$ with expansion factor 1).

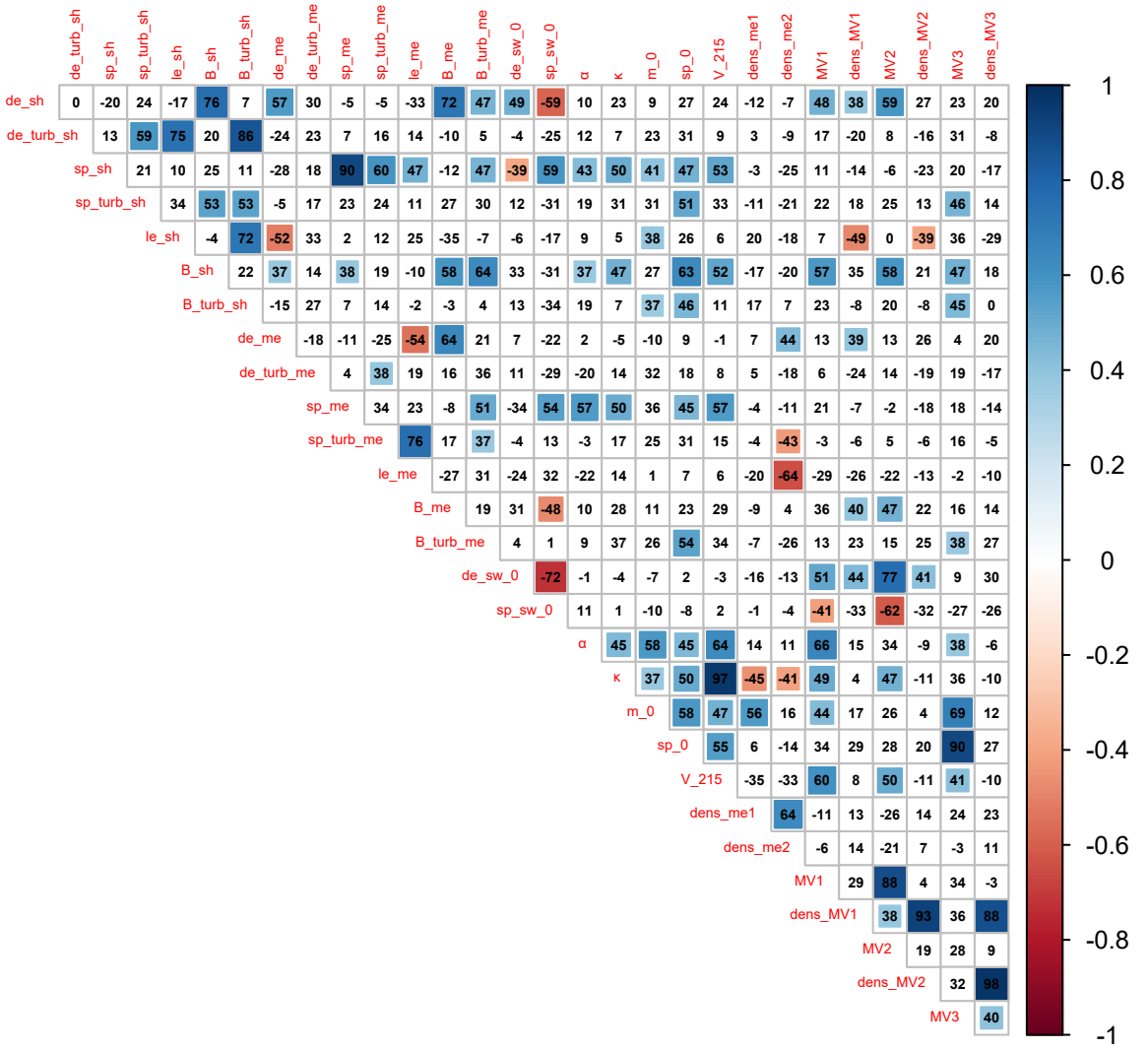

Figure 5.7: Correlation Matrix of the SHINE events. The value in the cells represents the percentage of the Pearson correlation coefficient. Correlations with p-values above 0.05 are considered as insignificant and are not color coded.

In the following we will discuss the results on the basis of different scatterplots.

Given in Figure 5.8 is the comparison between the two GCS parameters and their direct influence on the volume of the CME. We conclude that with R = 0.97 the aspect ratio κ (blue color) is the more dominating parameter (the half-angle α (golden color) in comparison shows a correlation of R = 0.64). Another interesting correlation can be found between α and the excess mass. This could be due to the fact that the wider the CME the more magnetic field structures and with that plasma is involved in the reconnection process. Therefore, the wider the CME, the more mass it can include.

Figure 5.9 depicts the results of the remotely derived density of the different ICME regions compared to their measured counterparts. Figure 5.9a and 5.9b give the results for the calculated ME and sh-sh density, dens_me1 (golden

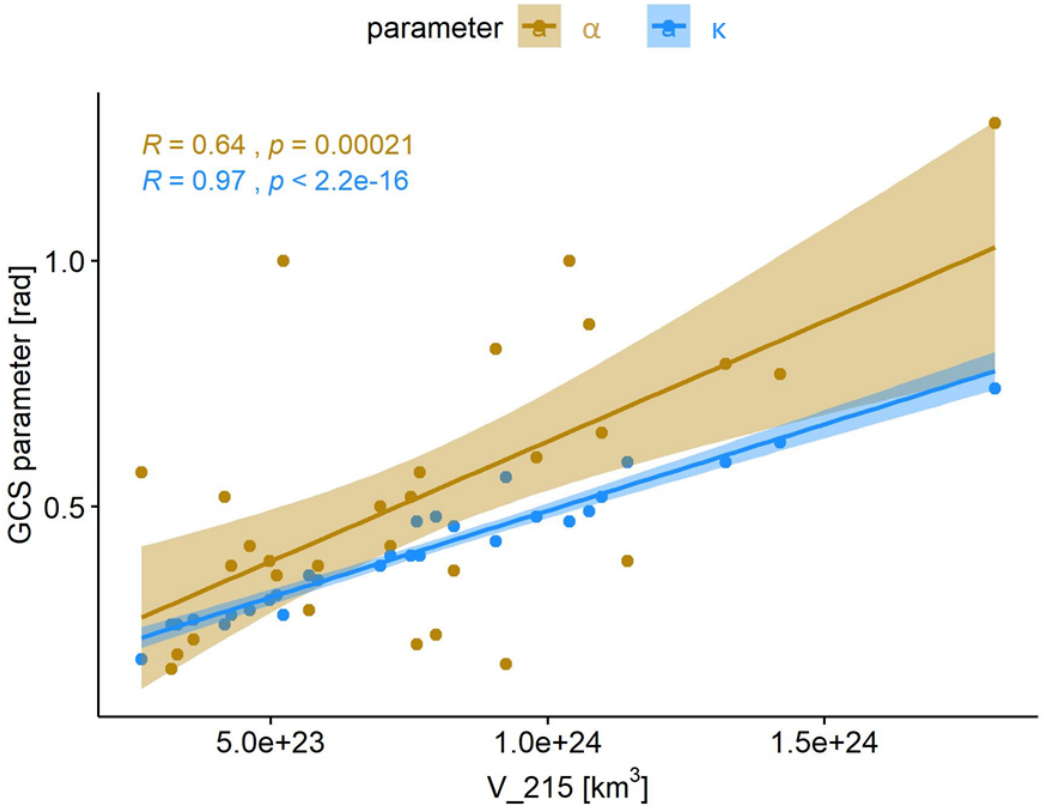

Figure 5.8: Comparison between the GCS parameters α and κ and their correlation to the derived GCS volume at 215 $R_\odot$. Similar to the plots in the previous section, the confidence interval corresponds to the accordingly colored shaded area.

color) and dens_MV2 (blue color) respectively. For the simplistic approach taken to calculate the ME density, we get no correlation at all. The calculated densities are on average too low, indicating that the assumed volume exceeds reasonable values. For the approach introduced by Cargill et al. (1996) (see Chapter 4.1.4 and Equation 4.15) taken for the sh-sh region we get a correlation coefficient R = 0.27. However, clearly visible in Figure 5.9a is an outlier with a derived density of about 250 cm^{-3}. An improvement for the correlation can be achieved by removing events that produce unreasonably large densities above 45 cm^{-3}. Hence, we obtain for the sh-sh density (dens_MV2) a, on a 95% level ($p < 0.05$), significant correlation coefficient R = 0.44. The lower panel (Figure 5.9c and 5.9d) shows results for dens_me2 (ME region) and dens_MV1 (sh-sh). We notice a much larger correlation (R = 0.44) in the ME region using the reduced volume as introduced in Chapter 4.2.1. For the sh-sh region we use the density dens_MV1 calculated from MV_{shell} and $V_{\text{sh-sh}}$ (see Equations 4.18 and 4.24 respectively) and obtain a correlation coefficient R = 0.38. Again, we remove densities above 45 cm^{-3} and achieve a slight improvement of R = 0.41 for the sh-sh region.

Confirming our assumptions of a pile up mass determined sh-sh density we find

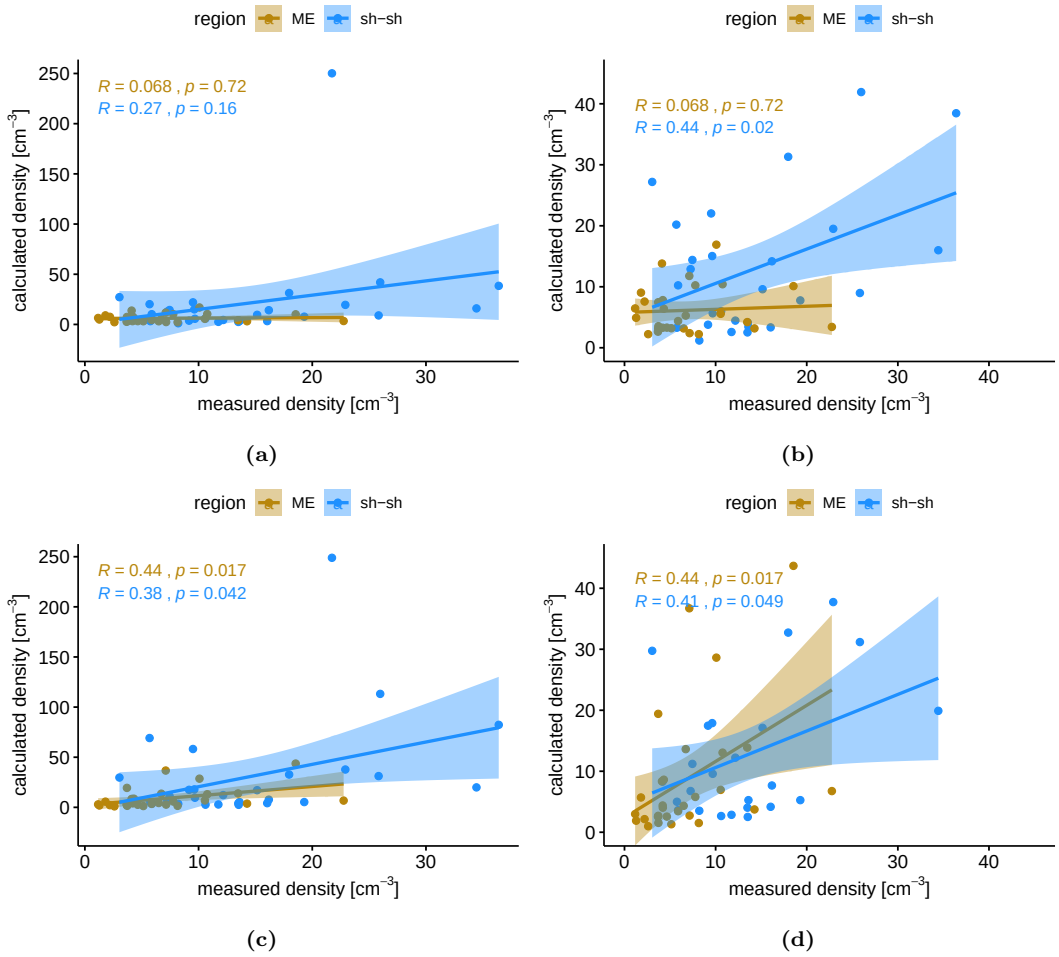

Figure 5.9: Comparison between the calculated and measured density. The left panel shows the results of all 29 events whereas in the right panel we remove events that produced calculated values above 45 cm^{-3}. In the upper panel we give the results for the ME and sh-sh region referring to the parameters dens_me1 and dens_MV2 respectively. For the lower panel we use dens_me2 and dens_MV1.

a positive correlation between the measured sh-sh density and the virtual mass MV1 and MV2 (see Figure 5.10a and 5.10b). Both methods lead to reasonable correlations. With R = 0.59, MV2 seems to be performing slightly better. In contrast to MV1 and MV2, MV3 does not correlate significantly with the sh-sh density and thus represents the least promising method. This becomes understandable once having a look at Table .2. Due to the simple calculation via conservation of momentum (see Equation 4.19), negative values for MV3 are possible when v_0 exceeds $v_{\mathrm{sh-sh}}$. A moderate positive correlation (R = 0.49) can be determined between the sh-sh density and the ambient solar wind density (see Figure 5.10c).

For the sh-sh density being positively correlated with the sh-sh magnetic field, we expectedly find correlations of the sh-sh magnetic field and the virtual mass MV1 and MV2 (shown in Figure 5.11a and 5.11b respectively). They show

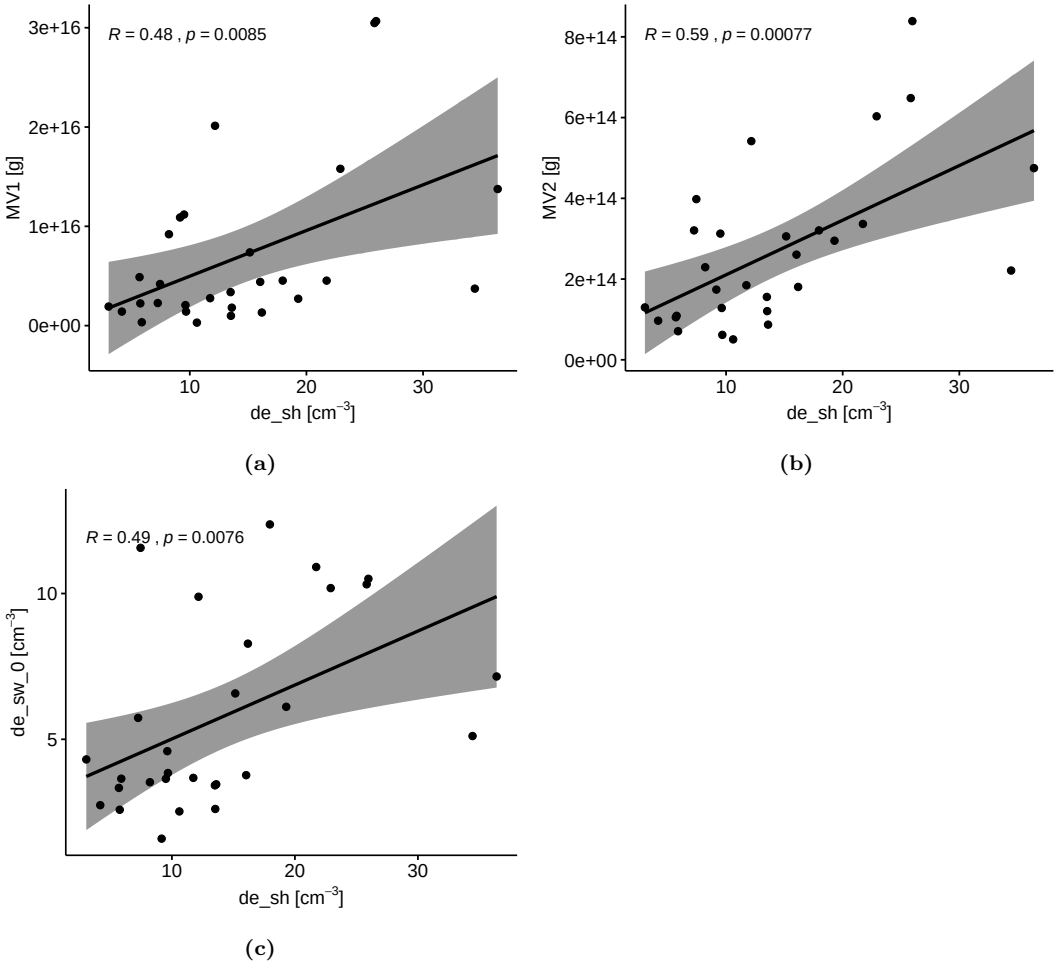

Figure 5.10: Correlations between the sh-sh density and different parameters. Upper panel: Correlation to the virtual mass as calculated by the two methods MV1 and MV2. Lower panel: Correlation to the ambient solar wind density.

similar correlation coefficients R of almost 0.6 indicating that a higher pile up mass is related to an enhancement in the sh-sh magnetic field. Another interesting positive correlation is obtained between the sh-sh magnetic field and the ME magnetic field turbulence intensity (see Figure 5.11c).

In Figure 5.12 we present negative correlations between the density and other parameters. Figure 5.12a and 5.12b show that shorter ME and sh-sh regions lead to higher measured ME densities. Investigating Figure 5.7 however reveals that the calculated density dens_me2 is only (negatively) correlated to the ME length (R = −0.64). The correlation can be improved to R = −77 by scaling the ordinate axis logarithmically meaning that the curve follows an exponential decrease rather than a linear one (Figure 5.12c). The same applies for the correlation between the sh-sh density dens_MV1 and the sh-sh length. Here we can improve the correlation from a linear (R = −0.49) to an exponential one even more substantially leading to R = −0.77 (see Figure 5.12d). Negative correlations can be furthermore found between the measured sh-sh density and

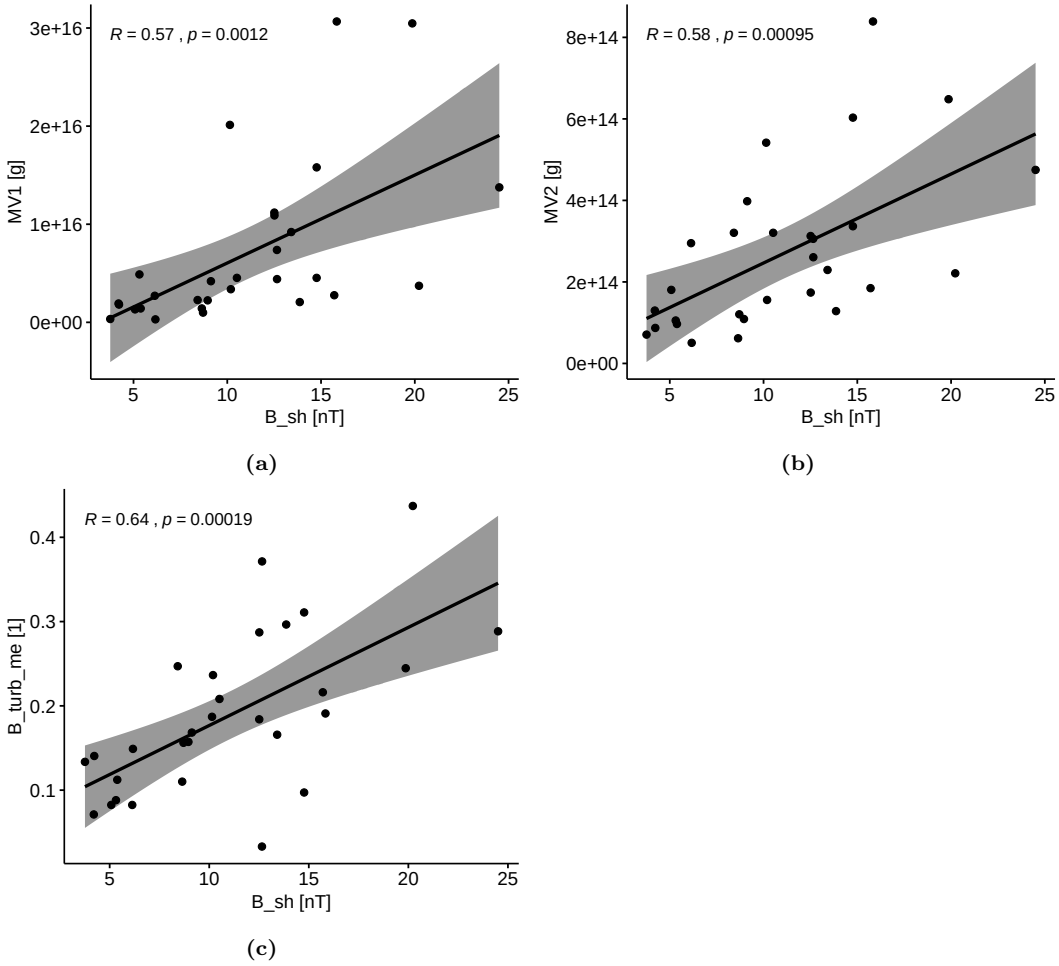

Figure 5.11: Correlations between the sh-sh magnetic field and different parameters. Upper panel: Correlation to the virtual mass as calculated by the two methods MV1 and MV2. Lower panel: Correlation to the turbulence intensity in the ME magnetic field.

the ambient solar wind speed with an exponential correlation coefficient of R $= -0.6$ (see Figure 5.12e) and between the ambient solar wind density and speed. This unsurprising linear correlation (R $= -0.72$) is directly related to the properties of the different solar wind streams already discussed in Chapter 2.2 and Table 2.1. Faster streams are accompanied by lower densities.

Relations of the initial CME speed and the sh-sh magnetic field and its turbulence intensity are depicted in Figure 5.13a and 5.13b. One additionally finds a positive correlation between the initial CME speed and the ME speed, the sh-sh speed and its turbulence intensity being largest for sp_turb_sh with R $=$ 0.51 (see Figure 5.7 and Figure 5.6c). Larger CMEs show significant correlations with the initial speed, the excess mass m_0, the measured speed in both regions (sp_me and sp_sh) and the sh-sh magnetic field (see Figure 5.7). As an example we present the largest of these correlations (sp_me) with R $= 0.57$ in Figure 5.13d. These correlations could hint towards the CME initiation process

on the Sun. The correlation of the CME volume and initial speed is also related to the flare reconnection flux (Dissauer et al., 2019). The same correlation as in the previous section (Chapter 5.1) with an even higher coefficient R = 0.76, can be found between the ME speed turbulence intensity and the ME length.

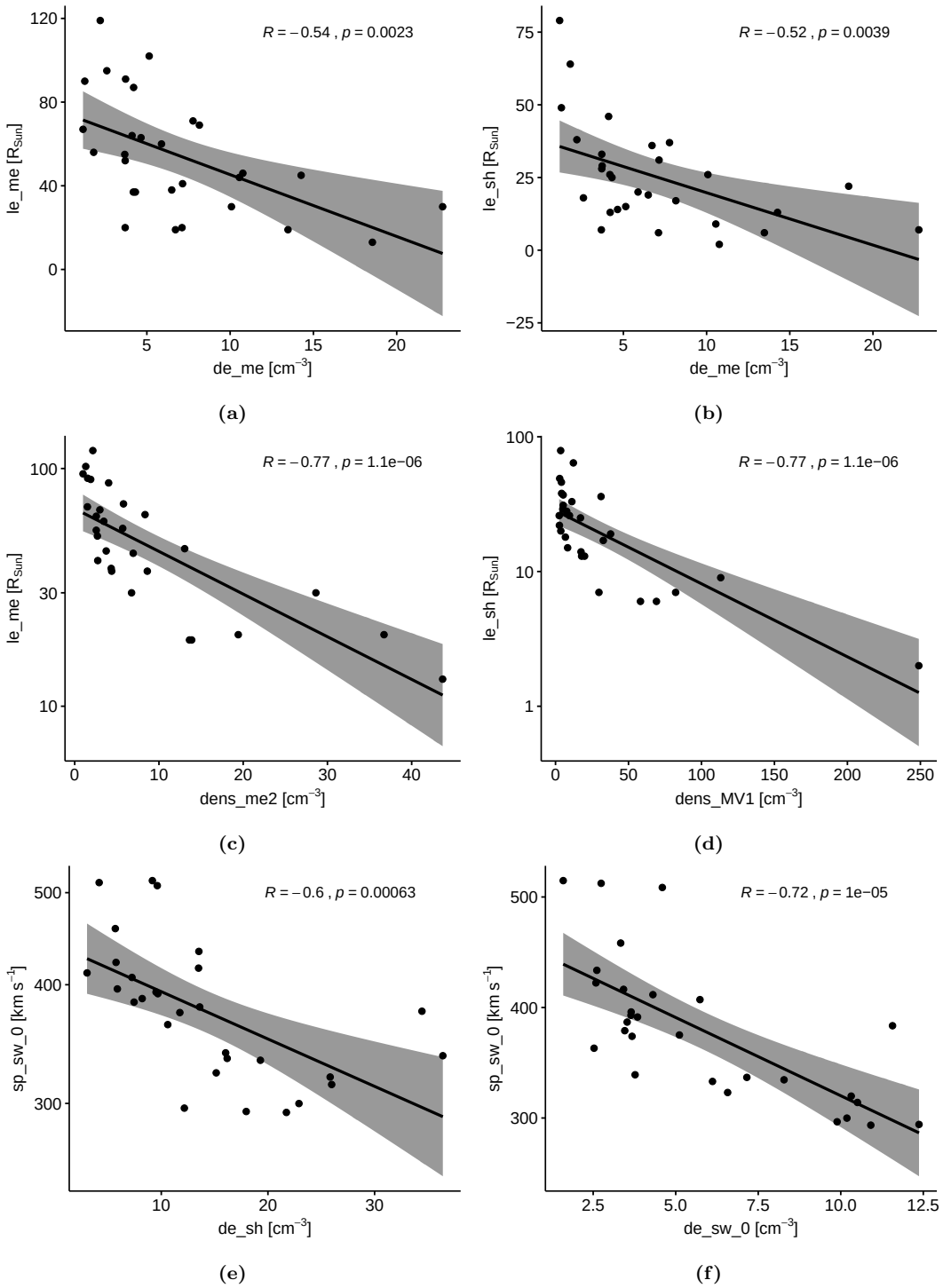

Figure 5.12: Upper panel left: Correlation between the ME density de_me and the ME length. Upper panel right: Correlation between the ME density de_me and the sh-sh length. Middle panel left: Correlation between the calculated ME density and the ME length (note the logarithmic scale of the ordinate axis). Middle panel right: Correlation between the calculated sh-sh density dens_MV1 and the logarithmic sh-sh length. Lower panel left: Correlation between the sh-sh density and the logarithmic ambient solar wind speed. Lower panel right: Correlation between the ambient solar wind density and the ambient solar wind speed.

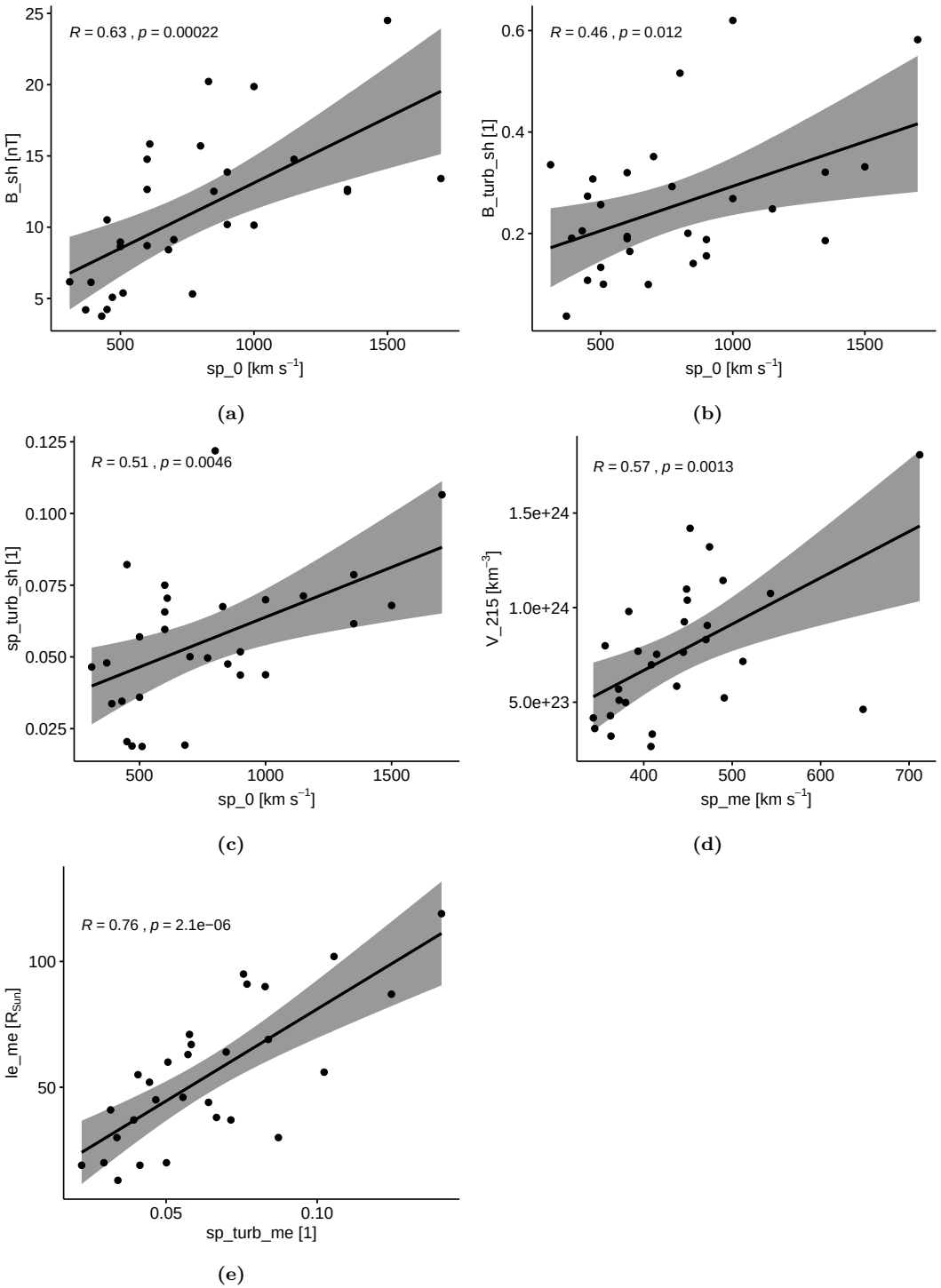

Figure 5.13: Upper panel left: Correlation between the initial CME speed and the sh-sh magnetic field. Upper panel right: Correlation between the initial CME speed and the sh-sh magnetic field turbulence intensity. Middle panel left: Correlation between the initial CME speed and the sh-sh turbulence intensity. Middle panel right: Correlation between the ME speed and the according CME volume at 215 $R_{\odot}$. Lower panel: Correlation between the ME speed turbulence intensity and the ME length.

6 Summary and conclusion

In this thesis we presented a straightforward and comprehensible method to derive CME densities from combined remote and in-situ observations. The method shows a way how to derive the geometry and consequently the volume from the 3D GCS reconstruction. Furthermore, we obtained the 3D CME mass from white light observations which enabled us to derive the excess density by simply dividing mass by volume. For the further CME density propagation in interplanetary space we assumed that a CME basically consists of the same parts as its interplanetary counterpart (ICME signatures; cf. Chapter 2.3 and Figure 2.9). On the one hand this is the closed flux rope part in which we assume the entire excess mass to be located and evenly distributed. On the other hand it consists of the frontal part with the leading shock front where we assume the available solar wind mass to be piled up in front of it. Hence, we deal with two separate masses (i.e. densities) which we can apply to our density calculations. That is, we can directly compare the measured and derived densities in the sh-sh (density derived from the pile up mass) and the ME (density derived from the excess mass) region. We presented different ways of computing the geometry expansion (keyword expansion factor; see also Equation 4.12), the considered volume (simplistic approach vs. ICME assigned volumes; cf. Chapter 4.1.3 vs. 4.2.1) and the pile up mass (i.e. virtual mass cf. Chapter 4.1.4).

From the analysis presented in Chapter 5, we conclude that our density deriving methods fail to provide definite predictions. Nevertheless, our results uncover certain trends and correlations that suggest our assumptions to be in accordance with measurements. However, due to the subjective nature of observational studies all calculations that are built on these are afflicted with large uncertainties. Regardless of this fact we can manifest some of our initial assumptions based on the results of this study:

- The mass in the flux rope part of the CME can be regarded as the corresponding measured mass within the ME region. That is, there is most likely little mass loss or gain within this region in interplanetary space.
- The mass in the shock-sheath region most probably refers to piled up solar wind material.
- The CME width represents a dominant property for the mass pile up in interplanetary. Hence, picturing the CME as a wedge-plow (or piston-type driver) might be a reasonable assumption.

List of Figures

List of Tables

Appendix

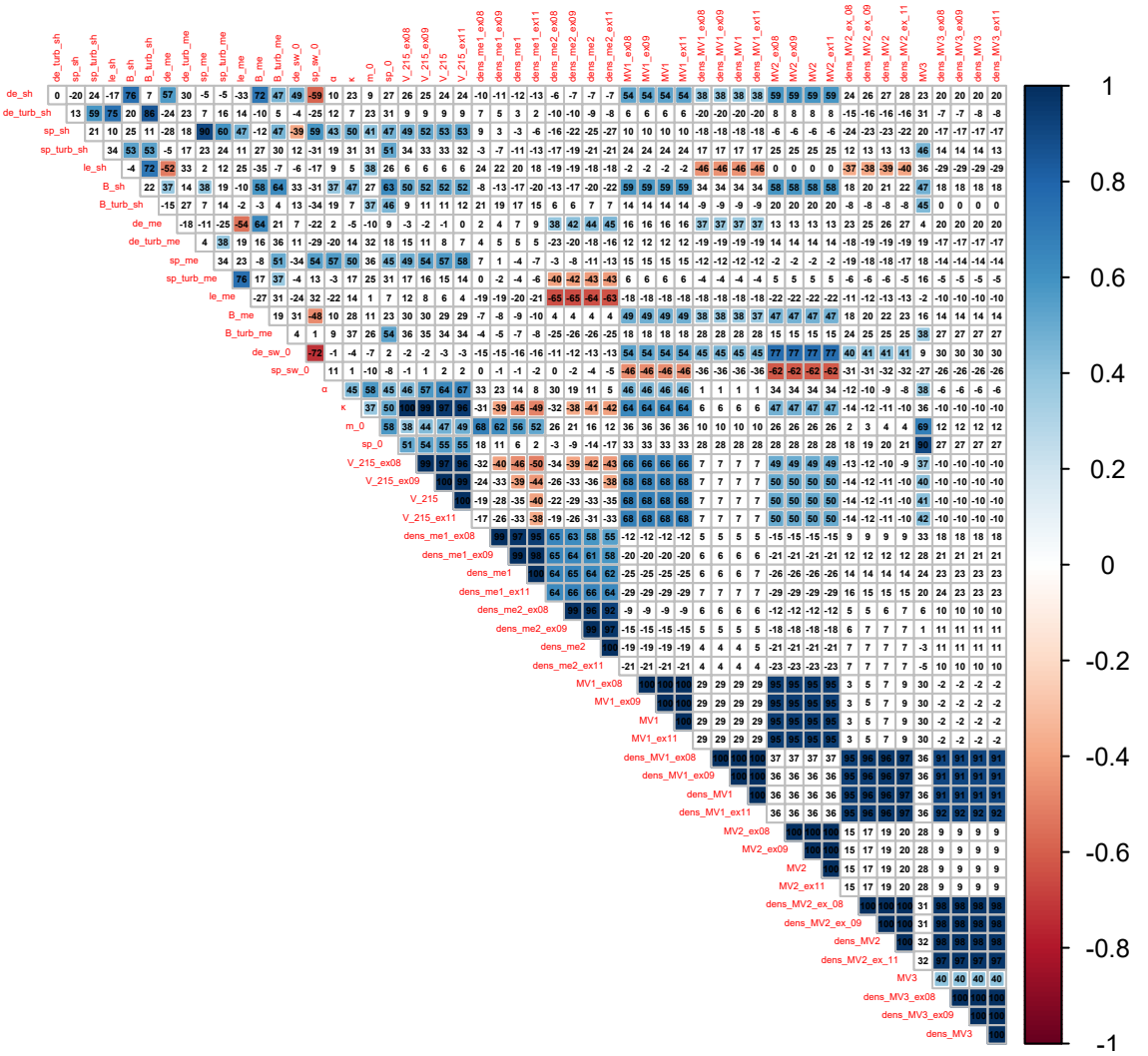

Figure .1: Extended correlation matrix generated from events given in the SHINE list.

Table .1: Exemplary parameters for the 125 *HELCATS Wind* events. sh-sh_start depicts the start of the ICME sh-sh region whereas the other parameters have the same nomenclature as explained in Chapter 5.1

sh-sh_start [dd-mmm-yy hh:mm]	de_sh [cm^{-3}]	sp_sh [km s^{-1}]	B_sh [nT]	de_me [cm^{-3}]	sp_me [km s^{-1}]	B_me [nT]
14-Jan-07 11:31	1.2	312.6	7.3	4.5	359.4	11.3
19-Nov-07 17:22	22.1	428.5	7.2	11.9	465.7	17.8
25-Dec-07 15:14		379.7	1.4	5.7	351.6	4.2
17-Sep-08 00:43	2.7	482.6	3.1	3.3	411.2	5.6
04-Dec-08 11:59	6.0	432.0	5.7	4.2	390.6	7.0
02-Jan-09 02:49	2.8	397.5	4.3	3.0	407.9	6.1
03-Feb-09 19:11	12.2	352.6	8.9	15.4	355.8	9.7
11-Mar-09 22:04	15.8	337.1	6.6	9.3	359.5	11.6
05-Apr-09 16:04	5.6	360.4	3.7	3.4	397.4	4.8
22-Apr-09 11:16	3.1	400.5	2.7	3.4	392.1	3.5
03-Jun-09 13:40	15.4	311.0	4.7	6.8	312.4	5.3
27-Jun-09 11:02	7.5	403.0	5.2	6.4	389.8	7.6
01-Nov-09 08:26	16.9	338.7	2.3	7.7	348.8	5.8
12-Dec-09 04:47	11.7	283.3	5.2	14.2	272.0	6.0
01-Jan-10 22:04	12.7	299.4	6.4	8.3	286.4	6.6
07-Feb-10 18:04	7.1	403.6	5.9	6.5	363.4	8.3
05-Apr-10 07:55	8.7	699.0	12.7	3.9	640.3	9.1
11-Apr-10 12:28	9.2	427.2	8.0	10.0	411.8	10.7
18-May-10 02:23	7.4	349.9	3.5	8.8	354.8	7.5
28-May-10 02:23	18.9	367.6	6.1	7.0	355.0	13.3
21-Jun-10 03:35	8.4	402.8	4.3	5.7	363.9	6.0
03-Aug-10 17:11	10.3	572.4	10.9	12.3	571.4	14.3
25-Sep-10 11:45	1.4	586.9	2.7	1.8	480.3	2.9
31-Oct-10 02:09	20.9	366.9	4.8	7.7	343.1	8.7
19-Dec-10 20:23	14.1	379.3	5.1	8.5	384.7	7.3
24-Jan-11 06:43	10.9	383.3	4.2	7.8	345.6	6.2
04-Feb-11 01:55	10.6	371.5	6.2	18.5	409.6	13.0
14-Feb-11 15:07	30.0	372.0	6.1	18.8	377.4	16.2
18-Feb-11 00:43	17.4	451.7	9.1	19.8	518.4	25.1
18-Feb-11 10:33	3.2	565.7	9.8	1.3	465.5	7.8
29-Mar-11 15:07	20.1	368.9	6.0	3.7	344.5	11.3
29-Apr-11 09:07	5.3	353.1	4.8	7.4	383.4	9.0
12-May-11 03:21	4.6	354.2	2.6	3.3	318.6	4.2
13-May-11 18:43	9.9	356.8	5.2	9.8	322.5	3.7
21-May-11 05:16	10.3	342.0	6.3	4.7	400.6	7.7
28-May-11 00:14	7.2	474.0	10.6	6.7	511.2	11.5
04-Jun-11 20:02	31.8	453.5	17.5	15.6	514.1	12.4
30-Jun-11 13:26	9.5	321.5	6.2	11.5	326.2	8.0
17-Sep-11 03:04	12.9	486.8	8.7	3.0	442.6	11.3
24-Oct-11 17:31	24.2	468.8	14.2	8.5	479.4	22.3

02-Nov-11 00:21	5.8	379.8	6.2	3.5	371.3	5.7
04-Nov-11 19:55	5.9	325.3	4.0	4.1	312.3	6.5
07-Nov-11 06:57	10.7	326.8	5.1	7.8	345.8	9.5
02-Jan-12 01:11	8.0	361.0	5.6	5.3	383.4	8.8
22-Jan-12 06:57	37.0	424.4	24.6	26.4	409.4	20.9
14-Feb-12 07:11	10.3	391.7	6.5	5.7	379.7	8.4
26-Feb-12 20:52	13.5	461.6	6.6	6.2	437.3	11.3
06-Mar-12 15:28	7.9	372.9	5.0	11.0	505.0	11.0
08-Mar-12 10:38	11.5	673.6	11.8	3.7	676.8	14.5
12-Mar-12 08:23	18.0	479.6	11.1	2.0	691.8	9.6
15-Mar-12 12:28	8.7	678.5	10.9	4.4	702.4	9.3
05-Apr-12 14:23	11.1	349.7	7.4	9.7	337.4	10.2
23-Apr-12 02:09	22.9	378.9	10.4	12.6	374.5	14.6
03-May-12 02:24	15.0	298.7	5.5	4.7	310.7	6.5
08-May-12 15:57	11.1	339.5	8.2	18.3	381.5	13.8
16-May-12 12:28	6.9	401.4	4.4	5.7	370.3	9.1
11-Jun-12 02:52	3.9	399.7	6.0	3.3	409.9	8.8
16-Jun-12 09:07	16.5	405.9	10.3	23.1	455.3	31.3
08-Jul-12 07:58	10.7	425.1	9.4	6.4	411.5	11.0
14-Jul-12 17:59	16.0	610.9	12.6	2.8	519.2	19.6
12-Aug-12 12:37	11.1	356.7	6.2	6.3	380.9	10.7
18-Aug-12 03:25	11.0	379.6	6.8	8.8	386.9	11.0
04-Sep-12 21:57	7.9	495.9	10.4	5.9	508.5	11.1
06-Sep-12 00:25	16.3	440.5	5.8	2.7	427.4	9.7
30-Sep-12 10:26	14.1	308.8	6.2	11.4	382.0	16.3
08-Oct-12 04:19	15.2	368.9	12.4	5.2	397.5	15.1
12-Oct-12 08:25	5.6	514.8	5.5	2.3	479.3	10.4
31-Oct-12 14:23	22.6	340.8	8.9	10.7	343.3	11.1
12-Nov-12 22:04	21.9	410.0	14.0	6.2	381.7	21.0
23-Nov-12 20:49	13.5	381.5	11.0	9.9	381.3	11.7
16-Jan-13 23:31	25.2	404.8	9.6	4.9	387.1	12.5
18-Jan-13 22:47	11.5	440.0	6.5	5.1	428.8	4.5
19-Jan-13 16:47	10.7	423.9	4.3	4.6	428.6	6.6
17-Mar-13 05:31	9.1	661.0	12.1	5.2	625.3	11.3
13-Apr-13 22:19	13.3	491.2	10.0	4.1	416.0	9.8
30-Apr-13 08:52	7.0	388.1	8.2	6.7	393.7	9.9
14-May-13 02:23	8.4	367.3	5.1	8.4	362.8	8.1
19-May-13 22:33	13.7	412.2	11.4	9.2	388.5	7.8
06-Jun-13 02:09	5.0	488.8	6.0	5.8	434.6	10.6
27-Jun-13 14:23	12.3	435.7	7.2	8.0	390.7	11.2
05-Jul-13 02:23	9.1	357.0	6.7	7.4	332.5	10.0
12-Jul-13 16:47	5.7	476.3	8.8	3.7	408.9	12.3
18-Jul-13 12:57	12.9	476.3	12.5	5.6	512.5	10.6
04-Aug-13 16:04	6.3	484.1	10.8	1.5	459.2	4.6
09-Aug-13 18:14	4.7	462.6	5.8	5.8	418.3	6.5

01-Sep-13 06:14	2.9	526.5	4.7	1.4	495.3	4.0
02-Sep-13 01:56	4.1	479.4	4.3	5.6	399.2	4.8
24-Sep-13 05:02	12.6	395.1	6.9	3.5	404.5	3.4
02-Oct-13 01:11	16.6	575.7	12.3	3.8	595.7	5.8
03-Oct-13 00:00		416.1		0.6	489.8	8.0
29-Oct-13 09:35	11.4	328.6	8.0	7.0	345.1	8.9
08-Nov-13 21:07	10.6	408.3	5.8	19.1	407.7	11.9
23-Nov-13 00:14	6.6	308.6	6.9	6.8	356.0	8.4
30-Nov-13 20:23	4.0	491.3	9.5	1.3	414.6	8.6
08-Dec-13 07:33	3.4	620.9	5.1	1.9	552.3	5.0
14-Dec-13 00:43	9.3	465.8	8.8	2.2	462.1	7.4
24-Dec-13 20:36	11.3	308.7	5.5	10.8	303.6	10.4
21-Jan-14 16:19	15.1	352.6	8.2	5.5	453.7	10.2
05-Feb-14 12:50	3.6	384.8	9.0	2.4	370.8	6.4
07-Feb-14 16:16	19.7	432.6	10.7	6.8	414.3	8.1
15-Feb-14 12:46	31.0	427.1	10.6	18.1	393.8	14.7
18-Feb-14 05:59	6.7	404.2	5.2	5.4	419.0	10.7
19-Feb-14 11:59	10.3	476.8	9.0	6.8	515.5	10.3
05-Apr-14 09:58	18.2	471.5	7.9	8.8	374.9	11.4
10-Apr-14 11:59	1.7	401.6	3.5	2.7	390.1	4.2
20-Apr-14 10:20	6.7	637.1	8.7	4.5	549.4	5.7
22-May-14 22:33	9.1	384.2	12.3	5.0	475.1	10.7
07-Jun-14 16:19	20.8	458.0	13.8	9.3	537.2	11.6
22-Jun-14 18:28	3.0	383.8	3.6	3.1	354.7	2.9
29-Jun-14 16:47	11.9	349.0	5.3	11.3	347.9	8.6
03-Jul-14 00:00	15.2	332.2	3.5	8.9	322.7	5.7
19-Aug-14 06:00	17.9	369.5	10.2	6.8	350.7	14.1
26-Aug-14 02:40	17.3	281.3	5.0	14.6	305.5	13.1
12-Sep-14 15:07	17.2	598.8	19.6	4.8	632.9	21.3
07-Jan-15 05:38	11.4	451.0	8.7	15.5	448.8	17.8
28-Mar-15 03:36	9.8	400.1	8.3	13.2	393.2	12.1
31-Mar-15 07:32	16.3	385.2	13.4	10.1	399.0	12.3
09-Apr-15 09:09	15.7	374.6	10.9	16.0	391.9	15.5
06-May-15 00:56	17.8	454.1	13.5	10.0	421.9	13.2
08-May-15 02:52	16.6	389.3	4.9	7.1	382.1	6.6
10-May-15 08:23	9.3	385.0	7.5	8.3	360.9	11.2
22-Jun-15 18:07	31.5	649.3	26.1	2.2	600.1	11.0
07-Sep-15 13:05	6.3	578.5	9.7	12.7	470.2	14.8
24-Oct-15 17:59	13.9	463.7	7.5	3.8	395.6	5.8
06-Nov-15 17:46	6.7	606.6	15.4	2.4	507.1	15.6

Table .2: SHINE list events with important parameters derived from the GCS reconstruction and in-situ measurements.

LASCO time [yyyy/mm/dd UT]	α [rad]	κ [rad]	m_0 [g]	sp_0 [km/s]	ICME shock time [yyyy/mm/dd UT]	de_sh [cm-3]	sp_sh [km/s]	le_sh [Rsun]	B_sh [nT]	de_me [cm-3]	sp_me [km/s]	le_me [Rsun]	B_me [nT]	de_sw_0 [cm-3]	sp_sw_0 [km/s]	v_215 [km-3]	dens_me1 [cm-3]	dens_me2 [cm-3]	MV1 [g]	dens_mv1 [cm-3]	MV2 [g]	dens_mv2 [cm-3]	MV3 [g]	dens_mv3 [cm-3]
2008/12/12 0525	0.23	0.27	4.50E+15	470	2008/12/16 1159	16	357	28	5	4	345	20	8	8	335	3.6E+23	7	19	1.3E+15	8	1.8E+14	14	1.4E+15	8
2009/12/16 0430	0.39	0.31	2.20E+15	370	2009/12/19 1000	3	427	7	4	4	379	55	4	4	412	5.0E+23	3	3	1.9E+15	30	1.3E+14	27	-2.9E+14	-5
2010/04/03 1033	0.42	0.29	6.04E+15	900	2010/04/05 0826	10	723	13	14	4	648	87	9	5	509	4.6E+23	8	4	2.1E+15	18	1.3E+14	15	1.5E+15	13
2010/04/08 0454	0.57	0.19	7.52E+15	500	2010/04/11 1304	10	428	26	9	10	408	30	11	4	391	2.7E+23	17	29	1.4E+15	10	6.2E+13	6	1.3E+15	8
2010/05/24 1406	0.24	0.48	3.20E+15	390	2010/05/28 0258	19	369	31	6	7	356	41	13	6	333	8.0E+23	2	3	2.7E+15	5	3.0E+14	8	1.8E+14	0
2010/06/16 0635	0.17	0.26	2.35E+15	430	2010/06/20 2000	6	391	20	4	6	363	60	6	4	396	3.2E+23	4	3	3.4E+14	4	7.1E+13	10	2.3E+14	2
2010/10/26 0200	0.52	0.26	7.14E+15	450	2010/10/30 1015	14	377	37	4	8	343	71	9	3	379	4.2E+23	10	6	1.8E+15	5	8.7E+13	3	1.4E+15	4
2011/01/30 2008	0.20	0.26	5.60E+15	310	2011/02/04 0155	11	372	22	6	19	410	13	13	3	363	3.3E+23	10	44	3.0E+14	3	5.1E+13	6	-9.3E+14	-8
2011/02/15 0236	0.37	0.46	6.83E+15	800	2011/02/18 0130	12	540	49	16	1	470	90	8	4	374	8.3E+23	5	2	2.8E+15	3	1.8E+14	3	3.3E+15	3
2011/03/03 0548	0.38	0.35	3.13E+15	510	2011/03/06 0331	4	531	15	5	5	437	102	5	3	512	5.8E+23	3	1	1.4E+15	8	9.7E+13	8	-1.2E+14	-1
2011/06/02 0745	0.42	0.40	3.80E+15	830	2011/06/04 2045	34	478	13	20	14	512	45	11	5	375	7.2E+23	3	4	3.7E+15	20	2.2E+14	16	2.8E+15	15
2011/06/14 0610	1.00	0.28	1.03E+16	770	2011/06/17 0241	6	530	6	5	7	491	20	8	3	458	5.2E+23	12	37	4.9E+15	69	1.1E+14	20	4.7E+15	66
2011/08/04 0412	0.87	0.49	1.16E+16	1700	2011/08/05 1751	8	544	79	13	1	543	67	5	4	387	1.1E+24	6	3	9.2E+15	4	2.3E+14	1	2.5E+16	9
2011/09/13 2210	0.22	0.47	4.20E+15	600	2011/09/17 0343	14	497	26	9	4	445	37	12	3	434	7.6E+23	3	4	9.9E+14	3	1.2E+14	4	8.7E+14	2
2011/10/22 0005	0.79	0.59	1.23E+16	610	2011/10/24 1831	26	484	9	16	11	474	44	20	11	314	1.3E+24	6	7	3.1E+16	113	8.4E+14	42	3.2E+15	12
2011/10/27 1200	0.29	0.36	3.01E+15	700	2011/11/01 0907	7	406	33	9	4	372	52	6	12	384	5.7E+23	3	3	4.2E+15	11	4.0E+14	14	2.2E+15	6
2011/11/26 0700	0.77	0.63	1.00E+16	1350	2011/11/28 2150	10	511	6	13	13	452	19	14	4	393	1.4E+24	4	14	1.1E+16	58	3.1E+14	22	1.6E+16	85
2012/01/19 1512	1.00	0.47	9.17E+15	1000	2012/01/22 0611	26	413	36	20	7	449	19	9	10	320	1.0E+24	5	14	3.0E+16	31	6.5E+14	9	1.3E+16	13
2012/03/13 1736	1.28	0.74	1.00E+16	850	2012/03/15 1306	9	714	14	13	5	712	63	9	2	515	1.8E+24	3	3	1.1E+16	17	1.7E+14	4	1.9E+15	3
2012/06/14 1412	0.65	0.52	6.28E+15	1500	2012/06/16 2019	36	495	7	25	23	448	30	31	7	337	1.1E+24	3	7	1.4E+16	82	4.7E+14	38	1.3E+16	76
2012/07/12 1648	0.39	0.59	1.45E+16	1350	2012/07/14 1809	16	615	38	13	2	490	119	16	4	339	1.1E+24	8	2	4.4E+15	4	2.6E+14	3	1.7E+16	16
2012/09/28 0000	0.36	0.32	8.89E+15	1150	2012/09/30 2305	22	378	2	15	11	372	46	14	11	294	5.1E+23	10	13	4.5E+15	249	3.4E+14	250	1.8E+16	998
2012/10/05 0724	0.57	0.40	8.24E+15	600	2012/10/08 0516	15	382	25	13	4	394	37	16	7	323	7.7E+23	6	9	7.4E+15	17	3.1E+14	10	4.7E+15	11
2012/11/09 1512	0.60	0.48	5.19E+15	600	2012/11/12 2311	23	421	19	15	6	383	38	21	10	300	9.8E+23	3	4	1.6E+16	38	6.0E+14	20	2.2E+15	5
2012/11/23 1336	0.18	0.56	3.45E+15	680	2012/11/26 0512	7	525	18	8	3	446	95	5	6	407	9.3E+23	2	1	2.3E+15	7	3.2E+14	13	1.0E+15	3
2013/04/11 0724	0.52	0.40	1.74E+16	900	2013/04/13 2254	13	495	46	10	4	415	64	10	3	416	7.5E+23	14	8	3.4E+15	4	1.6E+14	3	1.4E+16	17
2013/07/09 1512	0.50	0.38	4.13E+15	500	2013/07/12 1714	6	480	29	9	4	409	91	12	3	422	7.0E+23	4	2	2.2E+15	5	1.1E+14	3	1.8E+14	0
2013/09/29 2145	0.82	0.43	1.37E+16	1000	2013/10/02 0154	12	588	64	10	2	472	56	7	10	297	9.1E+23	9	6	2.0E+16	12	5.4E+14	4	9.6E+15	6
2014/08/15 1812	0.38	0.28	1.60E+15	450	2014/08/19 0657	18	367	17	11	8	362	69	16	12	294	4.3E+23	2	2	4.5E+15	33	3.2E+14	31	3.6E+14	3

Bibliography

Aschwanden, Markus J. (2005). *Physics of the Solar Corona. An Introduction with Problems and Solutions (2nd edition)* (cit. on pp. 5, 7).

Batchelor, G. K. (2000). *An Introduction to Fluid Dynamics* (cit. on p. 30).

Bein, B. M., M. Temmer, A. Vourlidas, A. M. Veronig, and D. Utz (May 2013). "The Height Evolution of the "True" Coronal Mass Ejection Mass derived from STEREO COR1 and COR2 Observations." In: *apj* 768, 31, p. 31. DOI: 10.1088/0004-637X/768/1/31. arXiv: 1303.3372 [astro-ph.SR] (cit. on pp. 21, 28).

Biermann, L. (Jan. 1951). "Kometenschweife und solare Korpuskularstrahlung." In: *ZAp* 29, p. 274 (cit. on p. 7).

Billings, Donald E. (1966). *A guide to the solar corona* (cit. on p. 28).

Bochsler, Peter (Mar. 2009). "Composition of matter in the heliosphere." In: *Universal Heliophysical Processes*. Ed. by N. Gopalswamy and D. F. Webb. Vol. 257. IAU Symposium, pp. 17–28. DOI: 10.1017/S1743921309029044 (cit. on p. 9).

Bothmer, V. and R. Schwenn (Jan. 1998). "The structure and origin of magnetic clouds in the solar wind." In: *Annales Geophysicae* 16.1, pp. 1–24. DOI: 10.1007/s00585-997-0001-x (cit. on p. 27).

Brueckner, G. E. et al. (Dec. 1995). "The Large Angle Spectroscopic Coronagraph (LASCO)." In: *solphys* 162, pp. 357–402. DOI: 10.1007/BF00733434 (cit. on p. 17).

Burkepile, J. T., A. J. Hundhausen, A. L. Stanger, O. C. St. Cyr, and J. A. Seiden (Mar. 2004). "Role of projection effects on solar coronal mass ejection properties: 1. A study of CMEs associated with limb activity." In: *Journal of Geophysical Research (Space Physics)* 109.A3, A03103, A03103. DOI: 10.1029/2003JA010149 (cit. on p. 11).

Burlaga, L. F. (May 2002). "Review of Magnetic Clouds/Flux Ropes and Types of Ejecta." In: *American Astronomical Society Meeting Abstracts #200*. Vol. 200. American Astronomical Society Meeting Abstracts, p. 65.12 (cit. on p. 16).

Burlaga, L. F., S. P. Plunkett, and O. C. St. Cyr (Oct. 2002). "Successive CMEs and complex ejecta." In: *Journal of Geophysical Research (Space Physics)* 107.A10, 1266, p. 1266. DOI: 10.1029/2001JA000255 (cit. on p. 16).

Cane, H. V. and I. G. Richardson (Apr. 2003). "Interplanetary coronal mass ejections in the near-Earth solar wind during 1996-2002." In: *Journal of Geophysical Research (Space Physics)* 108.A4, 1156, p. 1156. DOI: 10.1029/2002JA009817 (cit. on p. 16).

Cargill, P. J., J. Chen, D. S. Spicer, and S. T. Zalesak (Mar. 1996). "Magnetohydrodynamic simulations of the motion of magnetic flux tubes through a magnetized plasma." In: *J. Geophys. Res.* 101.A3, pp. 4855–4870. DOI: 10.1029/95JA03769 (cit. on pp. 30, 44).

Cargill, Peter J. (May 2004). "On the Aerodynamic Drag Force Acting on Interplanetary Coronal Mass Ejections." In: *Sol. Phys.* 221.1, pp. 135–149. DOI: 10.1023/B:SOLA.0000033366.10725.a2 (cit. on pp. 14, 30).

Chapman, Sydney and Harold Zirin (Jan. 1957). "Notes on the Solar Corona and the Terrestrial Ionosphere." In: *Smithsonian Contributions to Astrophysics* 2, p. 1 (cit. on p. 7).

Charbonneau, Paul (2014). "Solar Dynamo Theory." In: *Annual Review of Astronomy and Astrophysics* 52.1, pp. 251–290. DOI: 10.1146/annurev-astro-081913-040012. URL: ttps://doi.org/10.1146/annurev-astro-081913-040012 (cit. on p. 3).

Chen, J., C. Marque, A. Vourlidas, J. Krall, and P. W. Schuck (Sept. 2006). "The Flux-Rope Scaling of the Acceleration of Coronal Mass Ejections and Eruptive Prominences." In: *The Astrophysical Journal* 649.1, pp. 452–463. DOI: 10.1086/506466. URL: https://doi.org/10.1086%2F506466 (cit. on p. 24).

Chen, J., R. A. Santoro, J. Krall, R. A. Howard, R. Duffin, J. D. Moses, G. E. Brueckner, J. A. Darnell, and J. T. Burkepile (Apr. 2000). "Magnetic Geometry and Dynamics of the Fast Coronal Mass Ejection of 1997 September 9." In: *The Astrophysical Journal* 533.1, pp. 481–500. DOI: 10.1086/308646. URL: https://doi.org/10.1086%2F308646 (cit. on p. 24).

Chen, J. et al. (1997). "Evidence of an Erupting Magnetic Flux Rope: LASCO Coronal Mass Ejection of 1997 April 13." In: *The Astrophysical Journal Letters* 490.2, p. L191 (cit. on pp. 23, 24).

Colaninno, Robin C. and A. Vourlidas (June 2009). "First Determination of the True Mass of Coronal Mass Ejections: A Novel Approach to Using the Two STEREO Viewpoints." In: *ApJ* 698.1, pp. 852–858. DOI: 10.1088/0004-637X/698/1/852. arXiv: 0903.4344 [astro-ph.SR] (cit. on pp. 28, 29).

Cranmer, Steven R. (Sept. 2009). "Coronal Holes." In: *Living Reviews in Solar Physics* 6.1, 3, p. 3. DOI: 10.12942/lrsp-2009-3. arXiv: 0909.2847 [astro-ph.SR] (cit. on pp. 5, 6).

Cremades, H. and V. Bothmer (July 2004). "On the three-dimensional configuration of coronal mass ejections." In: *A&A* 422, pp. 307–322. DOI: 10.1051/0004-6361:20035776 (cit. on p. 11).

DeForest, C. E., T. A. Howard, and D. J. McComas (May 2013). "Tracking Coronal Features from the Low Corona to Earth: A Quantitative Analysis of the 2008 December 12 Coronal Mass Ejection." In: *ApJ* 769.1, 43, p. 43. DOI: 10.1088/0004-637X/769/1/43 (cit. on pp. 29, 30).

Dissauer, K., A. M. Veronig, M. Temmer, and T. Podladchikova (Apr. 2019). "Statistics of Coronal Dimmings Associated with Coronal Mass Ejections. II. Relationship between Coronal Dimmings and Their Associated CMEs."

In: *ApJ* 874.2, 123, p. 123. DOI: 10.3847/1538-4357/ab0962. arXiv: 1810.01589 [astro-ph.SR] (cit. on p. 48).

Esser, Ruth, Shadia R. Habbal, William A. Coles, and Joseph V. Hollweg (Apr. 1997). "Hot protons in the inner corona and their effect on the flow properties of the solar wind." In: *J. Geophys. Res.* 102.A4, pp. 7063–7074. DOI: 10.1029/97JA00065 (cit. on p. 9).

Foukal, Peter (2004). *Solar Astrophysics*. Weinheim: Wiley-VCH. ISBN: 3-527-40374-4 (cit. on pp. 4, 5).

Gosling, J. T. (July 1993). "Coronal mass ejections: The link between solar and geomagnetic activity." In: *Physics of Fluids B* 5.7, pp. 2638–2645. DOI: 10.1063/1.860701 (cit. on p. 1).

Hanslmeier, ARNOLD (2007). *THE SUN AND SPACE WEATHER: Second Edition*. Vol. 347. Astrophysics and space science library. Dordrecht, Berlin, and Heidelberg: Springer. ISBN: 9781402056031. DOI: 10.1007/978-1-4020-5604-8. URL: http://www.springerlink.com/content/m3mh62 (cit. on pp. 3, 6).

Holzknecht, L., M. Temmer, M. Dumbović, S. Wellenzohn, K. Krikova, S. G. Heinemann, M. Rodari, B. Vršnak, and A. M. Veronig (Jan. 2018). "CME volume calculation from 3D GCS reconstruction." In: *Central European Astrophysical Bulletin* 42, 3, p. 3 (cit. on pp. 25, 27).

Howard, R. A., D. J. Michels, Jr. Sheeley N. R., and M. J. Koomen (Dec. 1982). "The observation of a coronal transient directed at Earth." In: *ApJ* 263, pp. L101–L104. DOI: 10.1086/183932 (cit. on p. 12).

Howard, R. A., J. D. Moses, A. Vourlidas, J. S. Newmark, and D. G. Socker (Apr. 2008a). "Sun Earth Connection Coronal and Heliospheric Investigation (SECCHI)." In: *ssr* 136, pp. 67–115. DOI: 10.1007/s11214-008-9341-4 (cit. on pp. 13, 18).

Howard, T., ed. (2011). *Coronal Mass Ejections%*. Vol. 376. Astrophysics and Space Science Library. DOI: 10.1007/978-1-4419-8789-1 (cit. on p. 14).

Howard, T. A., D. Nandy, and A. C. Koepke (Jan. 2008b). "Kinematic properties of solar coronal mass ejections: Correction for projection effects in spacecraft coronagraph measurements." In: *Journal of Geophysical Research (Space Physics)* 113, A01104, A01104. DOI: 10.1029/2007JA012500 (cit. on p. 22).

Hundhausen, A. J. (Aug. 1993). "Sizes and locations of coronal mass ejections: SMM observations from 1980 and 1984-1989." In: *J. Geophys. Res.* 98.A8, pp. 13177–13200. DOI: 10.1029/93JA00157 (cit. on p. 11).

Kane, R.P. (Feb. 2002). "Some Implications Using the Group Sunspot Number Reconstruction." In: *Solar Physics* 205.2, pp. 383–401. ISSN: 1573-093X. DOI: 10.1023/A:1014296529097. URL: https://doi.org/10.1023/A:1014296529097 (cit. on p. 3).

Kasper, J. C., A. J. Lazarus, and S. P. Gary (Sept. 2002). "Wind/SWE observations of firehose constraint on solar wind proton temperature anisotropy." In: *grl* 29, 1839, p. 1839. DOI: 10.1029/2002GL015128 (cit. on p. 19).

Krieger, A. S., A. F. Timothy, and E. C. Roelof (Apr. 1973). "A Coronal Hole and Its Identification as the Source of a High Velocity Solar Wind Stream." In: *Sol. Phys.* 29.2, pp. 505–525. DOI: 10.1007/BF00150828 (cit. on p. 9).

Leblanc, Y., G. A. Dulk, and J.-L. Bougeret (Nov. 1998). "Tracing the Electron Density from the Corona to 1au." In: *solphys* 183, pp. 165–180. DOI: 10.1023/A:1005049730506 (cit. on p. 30).

Lemen, James R. et al. (Jan. 2012). "The Atmospheric Imaging Assembly (AIA) on the Solar Dynamics Observatory (SDO)." In: *Sol. Phys.* 275.1-2, pp. 17–40. DOI: 10.1007/s11207-011-9776-8 (cit. on p. 6).

Lepping, R. P., J. A. Jones, and L. F. Burlaga (Aug. 1990). "Magnetic field structure of interplanetary magnetic clouds at 1 AU." In: *J. Geophys. Res.* 95.A8, pp. 11957–11965. DOI: 10.1029/JA095iA08p11957 (cit. on p. 12).

Lepping, R. P. et al. (Feb. 1995). "The Wind Magnetic Field Investigation." In: *ssr* 71, pp. 207–229. DOI: 10.1007/BF00751330 (cit. on p. 19).

Lopez, R. E. (Oct. 1987). "Solar cycle invariance in solar wind proton temperature relationships." In: *J. Geophys. Res.* 92.A10, pp. 11189–11194. DOI: 10.1029/JA092iA10p11189 (cit. on p. 15).

McComas, D. J., S. J. Bame, P. Barker, W. C. Feldman, J. L. Phillips, P. Riley, and J. W. Griffee (July 1998). "Solar Wind Electron Proton Alpha Monitor (SWEPAM) for the Advanced Composition Explorer." In: *ssr* 86, pp. 563–612. DOI: 10.1023/A:1005040232597 (cit. on p. 18).

Mursula, K. and I. I. Virtanen (Aug. 2012). "The wide skirt of the bashful ballerina: Hemispheric asymmetry of the heliospheric magnetic field in the inner and outer heliosphere." In: *Journal of Geophysical Research (Space Physics)* 117.A8, A08104, A08104. DOI: 10.1029/2011JA017197 (cit. on p. 9).

Neugebauer, Marcia and Conway W. Snyder (Oct. 1966). "Mariner 2 Observations of the Solar Wind, 1, Average Properties." In: *J. Geophys. Res.* 71, p. 4469. DOI: 10.1029/JZ071i019p04469 (cit. on p. 7).

Parker, E. N. (Nov. 1958). "Dynamics of the Interplanetary Gas and Magnetic Fields." In: *ApJ* 128, p. 664. DOI: 10.1086/146579 (cit. on p. 7).

Parker, E. N. (Nov. 1960). "The Hydrodynamic Theory of Solar Corpuscular Radiation and Stellar Winds." In: *ApJ* 132, p. 821. DOI: 10.1086/146985 (cit. on p. 7).

Parker, E. N. (Sept. 1965). "Dynamical Theory of the Solar Wind." In: *Space Sci. Rev.* 4.5-6, pp. 666–708. DOI: 10.1007/BF00216273 (cit. on p. 8).

Priest, Eric and Terry Forbes (2000). *Magnetic Reconnection* (cit. on pp. 11, 13).

R Core Team (2017). *R: A Language and Environment for Statistical Computing*. R Foundation for Statistical Computing. Vienna, Austria. URL: https://www.R-project.org/ (cit. on p. 22).

Raith, Wilhelm (2001). *Band 7 Erde und Planeten*. De Gruyter. DOI: 10.1515/9783110198027 (cit. on pp. 8, 10).

Rankin, J. S., D. J. McComas, J. D. Richardson, and N. A. Schwadron (Sept. 2019). "Heliosheath Properties Measured from a Voyager 2 to Voyager 1 Transient." In: *ApJ* 883.1, 101, p. 101. DOI: 10.3847/1538-4357/ab3d9d (cit. on p. 8).

Richardson, I. G. and H. V. Cane (June 2010). "Near-Earth Interplanetary Coronal Mass Ejections During Solar Cycle 23 (1996 - 2009): Catalog and Summary of Properties." In: *solphys* 264, pp. 189–237. DOI: 10.1007/s11207-010-9568-6 (cit. on pp. 14, 21).

Riley, Pete, J. A. Linker, and Z. Mikić (July 2002). "Modeling the heliospheric current sheet: Solar cycle variations." In: *Journal of Geophysical Research (Space Physics)* 107.A7, 1136, p. 1136. DOI: 10.1029/2001JA000299 (cit. on p. 9).

Russell, C. T., A. A. Shinde, and L. Jian (Jan. 2005). "A new parameter to define interplanetary coronal mass ejections." In: *Advances in Space Research* 35.12, pp. 2178–2184. DOI: 10.1016/j.asr.2005.04.024 (cit. on p. 15).

Schwenn, R. (June 2006). "Solar Wind Sources and Their Variations Over the Solar Cycle." In: *Space Sci. Rev.* 124.1-4, pp. 51–76. DOI: 10.1007/s11214-006-9099-5 (cit. on pp. 9, 10).

Schwenn, R., A. dal Lago, E. Huttunen, and W. D. Gonzalez (Mar. 2005). "The association of coronal mass ejections with their effects near the Earth." In: *Annales Geophysicae* 23.3, pp. 1033–1059. DOI: 10.5194/angeo-23-1033-2005 (cit. on p. 11).

Skoug, R. M., J. T. Gosling, J. T. Steinberg, D. J. McComas, C. W. Smith, N. F. Ness, Q. Hu, and L. F. Burlaga (Sept. 2004). "Extremely high speed solar wind: 29-30 October 2003." In: *Journal of Geophysical Research (Space Physics)* 109.A9, A09102, A09102. DOI: 10.1029/2004JA010494 (cit. on p. 19).

Smith, C. W., J. L'Heureux, N. F. Ness, M. H. Acuña, L. F. Burlaga, and J. Scheifele (July 1998). "The ACE Magnetic Fields Experiment." In: *ssr* 86, pp. 613–632. DOI: 10.1023/A:1005092216668 (cit. on p. 18).

Tappin, S. J. (Feb. 2006). "The Deceleration of an Interplanetary Transient from the Sun to 5 Au." In: *Solar Physics* 233.2, pp. 233–248. DOI: 10.1007/s11207-006-2065-2 (cit. on p. 30).

Thernisien, A. (June 2011). "Implementation of the Graduated Cylindrical Shell Model for the Three-dimensional Reconstruction of Coronal Mass Ejections." In: *apjs* 194, 33, p. 33. DOI: 10.1088/0067-0049/194/2/33 (cit. on pp. 23, 24, 26).

Thernisien, A., R. A. Howard, and A. Vourlidas (Nov. 2006). "Modeling of Flux Rope Coronal Mass Ejections." In: *apj* 652, pp. 763–773. DOI: 10.1086/508254 (cit. on pp. 2, 21).

Thernisien, A., A. Vourlidas, and R. A. Howard (May 2009). "Forward Modeling of Coronal Mass Ejections Using STEREO/SECCHI Data." In: *solphys* 256, pp. 111–130. DOI: 10.1007/s11207-009-9346-5 (cit. on p. 21).

Thernisien, A., A. Vourlidas, and R. A. Howard (June 2011). "CME reconstruction: Pre-STEREO and STEREO era." In: *Journal of Atmospheric and Solar-Terrestrial Physics* 73, pp. 1156–1165. DOI: 10.1016/j.jastp.2010.10.019 (cit. on p. 2).

Vršnak, B., D. Ruždjak, D. Sudar, and N. Gopalswamy (Aug. 2004). "Kinematics of coronal mass ejections between 2 and 30 solar radii. What can be learned about forces governing the eruption?" In: *A&A* 423, pp. 717–728. DOI: 10.1051/0004-6361:20047169 (cit. on pp. 2, 14).

Vršnak, B. et al. (July 2013). "Propagation of Interplanetary Coronal Mass Ejections: The Drag-Based Model." In: *Sol. Phys.* 285.1-2, pp. 295–315. DOI: 10.1007/s11207-012-0035-4 (cit. on pp. 2, 30, 32).

Vršnak, B. et al. (June 2019). "Heliospheric Evolution of Magnetic Clouds." In: *The Astrophysical Journal* 877.2, 77, p. 77. DOI: 10.3847/1538-4357/ab190a. arXiv: 1904.08266 [astro-ph.SR] (cit. on p. 27).

Wenzel, K. P., R. G. Marsden, D. E. Page, and E. J. Smith (Jan. 1992). "The ULYSSES Mission." In: *A&AS* 92, p. 207 (cit. on p. 9).

Wilcox, John M. and Norman F. Ness (Dec. 1965). "Quasi-Stationary Corotating Structure in the Interplanetary Medium." In: *J. Geophys. Res.* 70.23, pp. 5793–5805. DOI: 10.1029/JZ070i023p05793 (cit. on p. 8).

Yashiro, S., N. Gopalswamy, S. Akiyama, G. Michalek, and R. A. Howard (Dec. 2005). "Visibility of coronal mass ejections as a function of flare location and intensity." In: *Journal of Geophysical Research (Space Physics)* 110.A12, A12S05, A12S05. DOI: 10.1029/2005JA011151 (cit. on p. 13).

Yashiro, S., N. Gopalswamy, G. Michalek, O. C. St. Cyr, S. P. Plunkett, N. B. Rich, and R. A. Howard (July 2004). "A catalog of white light coronal mass ejections observed by the SOHO spacecraft." In: *Journal of Geophysical Research (Space Physics)* 109, A07105, A07105. DOI: 10.1029/2003JA010282 (cit. on p. 11).

Yermolaev, Yu. I. et al. (July 2018). "Dynamics of large-scale solar-wind streams obtained by the double superposed epoch analysis. 4. Helium abundance." In: *arXiv e-prints*, arXiv:1807.03579, arXiv:1807.03579. arXiv: 1807.03579 [physics.space-ph] (cit. on p. 10).

Zhang, J., K. P. Dere, R. A. Howard, M. R. Kundu, and S. M. White (Sept. 2001). "On the Temporal Relationship between Coronal Mass Ejections and Flares." In: *ApJ* 559.1, pp. 452–462. DOI: 10.1086/322405 (cit. on p. 13).

Zurbuchen, Thomas H. and Ian G. Richardson (Mar. 2006). "In-Situ Solar Wind and Magnetic Field Signatures of Interplanetary Coronal Mass Ejections." In: *Space Sci. Rev.* 123.1-3, pp. 31–43. DOI: 10.1007/s11214-006-9010-4 (cit. on p. 16).